Investigation of a closed argon ICP

Tas, R.D.

Award date:
1996

Investigation of a closed argon ICP

R.D.Tas

VDF/NT 96

February 1996

Afstudeerverslag, februari 1996.
Report of Master's Degree graduation project, February 1996.

Eindhoven University of Technology
Faculteit der Technische Natuurkunde
Vakgroep Deeltjesfysica
Werkgroep Evenwichten en Transport in Plasma's

Hoogleraar: prof. dr. ir. D.C.Schram
Begeleiders: Joost van der Mullen en Hans de Regt

Contents

1 General introduction 1

2 A two dimensional CCD array for emission measurements 2
2.1 Introduction 2
2.2 Theory of the Absolute Line Intensity Method 2
2.3 McALI experimental set-up 2
2.3.1 Calibration of the experimental set-up 4
2.4 Comparison of the CCD camera, the photomultiplier and the photodiode system 7
2.4.1 Theory 8
2.4.2 Verification experiment 11
2.4.3 Results and Discussion 12
2.4.4 Conclusions 13
2.5 Detection limits McALI set-up 14
2.6 Conclusions regarding construction and implementation 14

3 Transition probability corrections by exploiting pLSE conditions 16
3.1 Introduction 16
3.2 Experimental 16
3.3 Method of determining transition probabilities 19
3.4 Results 20
3.5 Discussion 21
3.6 Conclusion 22

4 The closed argon ICP mapped 24
4.1 Introduction 24
4.2 The plasma source 24
4.3 Diagnostics 25
4.3.1 Absolute line emission intensities 25
4.3.2 Line emission during plasma power interruption 27
4.3.3 Diode laser absorption 29
4.3.4 Thomson scattering 31
4.3.5 H_β emission line broadening 32
4.4 Results 33
4.4.1 Thomson scattering 33
4.4.2 H_β emission line broadening 33
4.4.3 Power dependence 34
4.4.4 Filling pressure dependence 38
4.5 Conclusions 41

General Conclusions 43

Appendix 44

Dankwoord 46

1 General introduction

Inductively Coupled Plasmas (ICP) are widely used as stable plasma sources for fundamental plasma research, as diagnostical tool in analytical chemistry and in the deposition and etching industry. An other promising area of application is illumination, which is the field of interest in this graduation project.

The main aim of the project is to experimentally investigate closed inductively coupled ICP's for illumination purposes. On the road to this aim, three main stages can be distinguished. The first stage consists of the construction and implementation of an additional spectroscopic device for plasma observation based on a two dimensional CCD-array coupled to a monochromator, making it possible to observe a large number of spatially resolved line emission profiles across the plasma in one instant, and also observe generally very weak emission lines of highly excited states.

Soon after completion of the first stage, it became clear that the ability to accurately determine absolute population densities of highly excited states is essential to determine the important plasma parameters electron density and electron temperature. Knowledge of the transition probability of atomic transitions is essential in calculating population densities from line emission experiments. However, no accurate values for transition probabilities between highly excited states in the argon atomic system were available. This led to the second stage in the project: the determination of transition probabilities between highly excited states with improved accuracy. Because of its accessibility for diagnostics, an *open* argon ICP is chosen as plasma source in this stage.

The third stage of the project deals with the determination of spatially resolved important plasma parameters like electron density, electron temperature and heavy particle temperature of *closed* argon ICP's. Several diagnostical techniques are applied: absolute line emission intensities (ALI) using the improved transition probabilities, diode laser absorption (DLA), line intensities during plasma power interruption (LIPI) and Thomson scattering (TS). During this stage, we had intensive contacts with Philips Forschungslaboratorien Aachen (Germany) and Philips Lighting Eindhoven.

The three stages of the project can be found in this report as respectively chapters 1 - 3.

2 A two dimensional CCD array for emission measurements

2.1 Introduction

The Absolute line emission intensity method (ALI) is a well known diagnostic method to determine the population density of an atomic state in a plasma.
In this section, the construction, application and testing of a Multi channel Absolute Line Intensity device (McALI) is described. It allows the simultaneous determination of population densities at several positions in the plasma.

2.2 Theory of the Absolute Line Intensity method

ALI is based on the fact that the lifetime of an excited atomic state is limited. Therefore, after some time a transition occurs to a state with lower energy. The energy difference of those states can be found in the frequency of the photon that is emitted as a result of the transition. ALI detects the amount of photons emerging from a plasma volume. From this data and with knowledge of the average lifetime of the state, the density of atoms in the corresponding state in the plasma volume can be deduced according to

$$n_p = \frac{4\pi j_{pq}}{h\nu_{pq} A_{pq}}, \qquad (1)$$

with j_{pq} the wavelength integrated emissivity in $Wsr^{-1}m^{-3}$ of the observed electronic transition from level p to level q, $h\nu$ the photon energy in J, and A_{pq} the transition probability.
In general we will have an experimental setup that only detects an unknown fraction of the total amount of photons emitted by the plasma for a given transition. In order to determine this fraction, the setup has to be calibrated.

2.3 McALI experimental set-up

The experimental setup essentially used throughout this report whenever ALI or H_β measurements are performed, consists of a two dimensional CCD array mounted on a B&M 1m Czerny-Turner monochromator, on the place where usually the exit slit is positioned. The dispersive element in the monochromator is a 1200 lines/mm flat grating. At the exit of the monochromator, the horizontal dispersion is 0.83 nm/mm.
A top view of the setup is displayed in Figure 1. The setup consists of a set of lenses and mirrors that image the plasma on the entrance slit of the monochromator. The default

entrance slit width is 100 μm. The first and second lens of the optical system have focal lengths of 0.5 m, the third and forth 0.25 m. Their diameters are 5 cm.

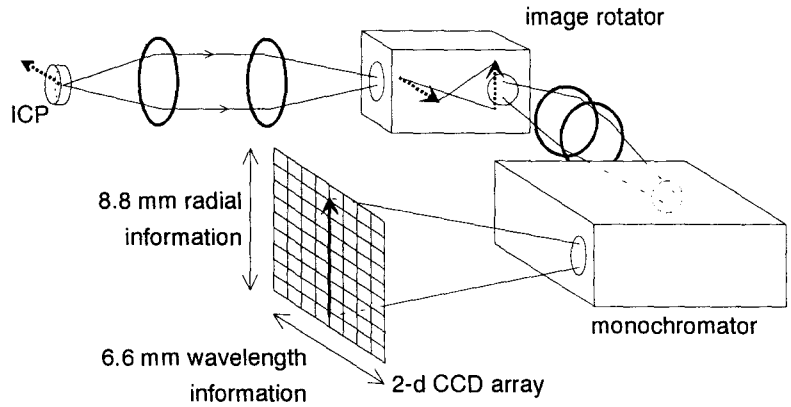

Figure 1. Top view of the McALI set-up. The closed ICP in this figure has cylindrical symmetry around the optical axis of the system. The arrows indicate the orientation of the image.

The closed ICP in this figure has cylindrical symmetry around the optical axis of the system, therefore making the presence of the image rotator not strictly necessary. However, in the second section of this report, the closed ICP is substituted by an open ICP which does not have this symmetry.

The ST6UV CCD detector is produced by SBIG, 'UV' indicating its spectral sensitivity well into the UV region. The camera is based on a Texas Instruments TI TC241 CCD chip. This CCD is a 'frame transfer CCD', meaning that when a picture is taken, this picture is quickly shifted to an CCD area covered by a metal coating. This area is equal in size to the sensitive area, and prevents the pictures to be locally over-exposed during the relatively slow readout session (ADC). The sensitive area is 6.6 mm horizontally x 8.8 mm vertically, consisting of 242 x 750 pixels. These pixels can be 'binned', effectively increasing pixel sizes in one or two dimensions. In every ALI experiment in this report, we have worked with 25 pixels vertically, and 242 pixels horizontally. This means the plasma is spatially resolved with an resolution of 0.352 mm. The (measured) dispersion in this case is 20 pm/pixel. In order to fully use this in experiments where optimal wavelength resolution is desired, the entrance slit of the monochromator needs to be smaller than 25 μm.

Because of some system astigmatism, the exit focal plane for optimal space resolution is not equal to the plane for optimal wavelength resolution. In every ALI experiment in this report, the camera has to be positioned in the plane of optimal spatial resolution, in order to get the 0.352 mm resolution. The wavelength resolution is then still better then 200 pm. In every H_β measurement in this report, the camera is placed in the plane of optimal wavelength resolution, and a 25 μm entrance slit is used. Note that for H_β measurements, the spatial resolution therefore is worse than 0.352 mm.

For every ALI measurement in this report, two pictures are taken. One with the camera shutter open, and one with the camera shutter closed. The latter is subtracted from the first. This procedure is necessary to correct for 'dark current', the number of counts the camera registers because of thermal effects. The dark current can be reduced by cooling of the CCD. In every experiment, the CCD camera was operated at -28°C.

Relevant information about a plasma emission line regarding ALI is the wavelength integrated number of detected counts of an emission line, indicated by the hatched surface in Figure 2. Integration of line emission minus continuum emission takes place over a selected CCD area corresponding with λ_{min} to λ_{max} by data processing software. The hatched area is related to energy emitted by the plasma in this line by an identical measurement with a Tungsten ribbon lamp; calibration of the experimental setup described in the next chapter.

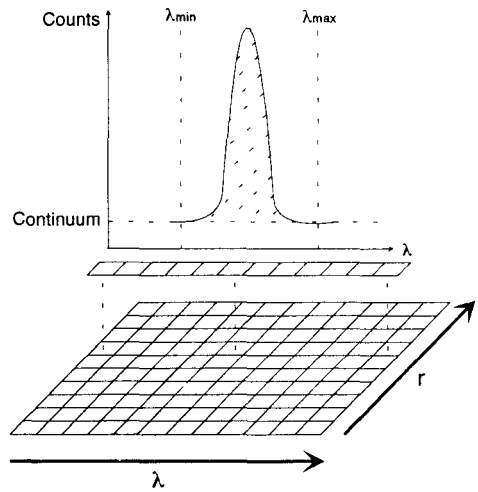

Figure 2. Determination of total number of counts in a detected emission line at one position in the plasma. The hatched surface under the emission line is the information of interest.

The camera is computer operated, and pictures are fed back into the computer by a serial cable. Communication with the camera takes place via RS232 at 115 Kbaud. A Pascal library of camera functions has been written (see appendix), and experimentation has been streamlined by a friendly user shell written by Jan van Dijk using Turbo Vision software

2.3.1 Calibration of the experimental setup

The ALI experimental setup detects an unknown fraction of photons emitted from a given plasma volume. In order to find out the relation between detected photons and actually emitted photons, calibration of the ALI setup is necessary. This calibration is performed with a Tungsten ribbon lamp, which itself is calibrated by an appropriate institute. Firstly, the essentials of the Tungsten ribbon calibration are explained, followed by the description of how atomic state population densities are determined with the ALI method.

2.3.1.1 The Tungsten ribbon lamp

When working with Tungsten ribbon lamps, the quantities 'true temperature' T_{true} and the 'radiance temperature' $T_{rad,\lambda}$ are often used. Their meaning is the as follows:

- T_{true} is the temperature of a source measured with a thermometer in perfect contact and thermal equilibrium with that source.
- $T_{rad,\lambda}$ of a source is the temperature of a black body that has the same emissivity as the source for a narrow spectral region around wavelength λ.

The relation between T_{true} and $T_{rad,\lambda}$ is expressed in

$$I(\lambda, T_{rad,\lambda}) = \tau \cdot \varepsilon(\lambda, T_{true}) \cdot I(\lambda, T_{true}) \tag{2}$$

with

$$I(\lambda, T_{rad,\lambda}) = \frac{2hc^2}{\lambda^5} \frac{1}{e^{\frac{hc}{\lambda k T_{rad,\lambda}}} - 1} \tag{3}$$

$$I(\lambda, T_{true}) = \frac{2hc^2}{\lambda^5} \frac{1}{e^{\frac{hc}{\lambda k T_{true}}} - 1} \tag{4}$$

where both of the latter spectral emissivities I have dimension $Wm^{-2}sr^{-1}m^{-1}$, τ represents the transmission coefficient of the transparent material surrounding the Tungsten ribbon (glass or quartz), $\varepsilon(\lambda, T_{true})$ is the known (tabelized) experimental emission coefficient of Tungsten at wavelength λ and true temperature T_{true} , h denotes planck's constant, k Boltzmann's constant and c the speed of light.
Very often $T_{rad,\lambda}$ is known (for example from the calibration report of the lamp), and one is interested in the corresponding value of T_{true}. From substitution of (4) and (3) in (2) we get the following equation

$$T_{true} = \frac{C_1}{\ln\left(\tau \cdot \varepsilon(\lambda, T_{true}) \cdot (e^{\frac{C_1}{T_{rad,\lambda}}} - 1) + 1\right)} \tag{5}$$

with $C_1 = \frac{hc}{\lambda k}$.

Since we need to know T_{true} to determine ε, the following iterative procedure is required:

- use $T_{rad,\lambda}$ as a first estimate of T_{true} to determine ε.
- use equation (5) to calculate T_{true} , use this T_{true} to determine a better value of ε, repeat till the successive values of T_{true} have stabilized within an acceptable range.

Having found T_{true},, the spectral emissivity of the Tungsten ribbon bulb is known and given by

$$I(\lambda, T_{true}) = \tau \cdot \varepsilon(\lambda, T_{true}) \frac{2hc^2}{\lambda^5} \frac{1}{e^{\frac{hc}{\lambda k T_{true}}} - 1}. \tag{6}$$

Of course this needs to be multiplied by $\Delta\lambda$ to obtain the amount of power emitted per square meter and per solid angle.
The number of photons actually emerging from the Tungsten ribbon in a small cone perpendicular to the ribbon per second per square meter per solid angle per $\Delta\lambda$ (Number $s^{-1}m^{-2}sr^{-1}m^{-1}$) is often denoted as the 'de Vos number' and can be expressed by

$$N_{deVos} = \varepsilon(\lambda, T_{true}) \frac{2c}{\lambda^4} \frac{1}{e^{\frac{hc}{\lambda k T_{true}}} - 1}. \tag{7}$$

For an example of how to use the Tungsten ribbon lamp in a practical situation, consider the optical system as used in the passive emission diagnostic branch. We want to determine the absolute population density per statistical weight η of a state in a plasma.
A Tungsten ribbon lamb is used with a current corresponding to $T_{rad,\ 662.4\ nm}$ = 1600 °C = 1873.15 K. Assume τ to be 0.92. With the iterative procedure outlined above, we find T_{true} = 2029.7 K.

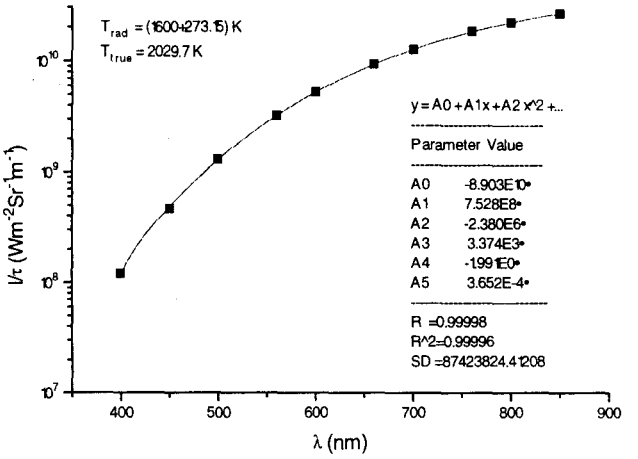

Figure 3. Graph of the spectral emissivity with a fifth order polynomial fit.

Now the spectral emissivity $I(\lambda, T_{true})$ can be calculated using equation (6). A graph of this quantity with a polynomial fit of order 5 is depicted in Figure 3.

2.3.1.2 Calibration of the setup and the atomic state population density with ALI

Consider a experimental setup where an one-to-one image of a Tungsten ribbon is projected on the entrance slit of a monochromator. The monochromator disperses in the horizontal plane. Suppose we only consider a small interval of the entrance slit with height h. This interval could be determined by the height of the detector at the exit of the monochromator. The width of the detector at the exit corresponds to a small wavelength interval $\Delta\lambda$.
With our detector we register the following amount of photons $N_{Tungsten}$ from the Tungsten ribbon

$$N_{Tungsten} = f \cdot \Omega \cdot \tau \cdot N_{deVos} \cdot \Delta\lambda \cdot b \cdot h_p, \tag{8}$$

where f is an unknown fraction, Ω is the solid angle determined by the entrance pupil and the focal length of the first lens of the system, $\Delta\lambda$ the considered wavelength interval, b the slit width and h_p the detector height. In case of McALI (see section 2.3), h should be interpreted as the height of a (binned) pixel.
Now the same setup is used to look at a plasma, which is placed with its center at the spot where the Tungsten ribbon was before. Suppose only one atomic emission line, much stronger than its underground, fits completely on the detector at the exit of the monochromator. If the line-of-sight thickness d of the plasma is small compared to the focal length of the first lens in the system, the amount of photons N_{plasma} caught from a plasma is

$$N_{plasma} = f \cdot \frac{\Omega}{4\pi} \eta \cdot g_u \cdot A_{ud} \cdot d \cdot b \cdot h_p. \tag{9}$$

η Is the density per statistical weight, g_u the statistical weight of the upper level of the transition, A_{ud} the transition frequency, and d the estimated plasma thickness.
Dividing (9) by (8) and re-arranging terms we finally find

$$\eta = \frac{4\pi \cdot \Delta\lambda \cdot \tau \cdot N_{deVos}}{A_{ud} \cdot g_u \cdot d} \frac{N_{plasma}}{N_{Tungsten}}. \tag{10}$$

2.4 Comparison of the CCD camera, the photomultiplier and the photodiode system

In this chapter three photon detection systems are compared that are commonly used in this group: 1) The SBIG ST6-UV 2-dimensional CCD camera (CCD), 2) the Reticon RL1024S Photo Diode Array (PDA) and 3) the Hamamatsu R376 Photon Multiplier Tube (PMT). The CCD camera is applied in ALI experiments, the PDA in Thomson experiments and the PMT in LIPI experiments.
A number of easy-to-use equations are derived, making a quick choice between the systems possible in some cases. However, since the systems considered are quite different, it is important to realize that in most cases a choice for a system will be based on reasons not within the scope of this report. For example, the number of detector dimensions needed can be a primary choice of system. The PMT consists of 1 sensitive area, the PDA of 1024 in a row, and the CCD of a grid of 242 x 375. At the same time, the system differences make general comparison impossible. To compare the systems it is necessary to make a three-fold distinction:

1. Quantum efficiency of the system.
2. Resolution and range of the ADC-unit.
3. Constant noise sources.
4. Dark current per detector surface.

1. Quantum efficiencies of the system.

In all of the above detection systems photons cause electrons on impact, and these are counted.
The Quantum efficiency (QE) is defined as the number of electrons created by a photon, and usually is a number between 0 and 1. It can also be interpreted as the chance that a photon 'caught' by the optical system will 'generate' an electron.

2. Resolution and range of the ADC-unit.

The second important point of comparison concerns the conversion of the collected number of electrons to a readable number of counts of some sort.
Two quantities are important:

- The number of electrons necessary for one count, known as the resolution.
- The maximum amount of counts that can be registered; the range.

3. Constant noise sources.

In the process of reading out the detectors noise can be introduced. This is often referred to as constant noise or readout noise. In case of the PDA and the CCD, the readout noise is caused by both ADC and by discharging an electron collection capacitor after an ADC. The PMT does not have an equivalent noise component.

4. Dark current per detector surface.

All of the detectors involved have 'dark current', that is electrons are collected even though they are not illuminated. This current decreases when the detector is cooled.

Dark current is proportional to detector surface. This makes it favorable if a sub-part of the detector surface is selectable when not all of the surface is needed in an experiment.

2.4.1 Theory

In the following we will make a distinction between a case of small and a case of large photon fluxes. We assume that it is possible in all systems to perform a measurement with the detector not illuminated, the so-called 'dark measurement', for the rest similar to the measurement *with* entering photons. We also assume the overall noise to have two components: a constant component and a shot noise component, equal to the square root of the collected number of electrons E_{coll}. Examples of constant noise are readout noise, reset noise and amplifier noise.

2.4.1.1 Photon detection limit; smallest detectable photon fluxes.

In the process of detecting small photon fluxes, we can distinguish three thresholds necessary for the number of collected photons to exceed in order to be detected.

1. Constant noise. The number of detector electrons due to collected photons needs to exceed the constant noise in order to be detectable. For the PMT we shall state that the number of photons has to be more than the QE to be detectable.
2. ADC resolution. The number of detector electrons due to collected photons needs to exceed the number of electrons necessary for one ADC count.
3. Shot noise. The number of detector electrons due to collected photons needs to exceed the shot noise in order to be detectable. Shot noise is proportional to the square root of the *total* amount of registered electrons.

The magnitudes of these thresholds have to be compared to the amount of shot noise due to dark current, the only threshold increasing with time. If this shot noise exceeds the thresholds, which is always the case after a certain amount of time, we can focus on the question of how large a photon flux is necessary to exceed this shot noise. In Table 1 the constant noise data and the ADC resolution data is expressed in dark current shot noise equivalent time t_{eq} . For short ($\Delta t < t_{eq}$) exposures to small photon fluxes, the thresholds can play an determining role.
In the following however we will assume that the measuring time $\Delta t > t_{eq}$. A good criteria for the minimum amount of detectable photons in a certain time of measuring Δt is then:

$$QE \cdot n > (\sqrt{E_{coll}^{light}} + C) - (\sqrt{E_{coll}^{dark}} + C) \approx 2 \cdot (\sqrt{E_{coll}^{dark}} + C) \quad \text{for } n \text{ small} \tag{11}$$

Here n is the amount of photons entering the detector during the measurement, E_{coll}^{light} is the amount of collected electrons, E_{coll}^{dark} the amount of collected electrons during the 'dark measurement' and C is the constant noise expressed in number of electrons. The idea behind this equation is that the signal needs to be higher than the noise in order to be able to detect it.
With a dark current of I_{coll}^{dark} (number of electrons/s), we collect $\Delta t^* I_{coll}^{dark}$ 'dark electrons' per measure time Δt. In order to fulfill (11), and assuming a constant photon flux ψ_{coll}^{light}, we find the detection limit for this flux

$$\psi_{coll}^{light} > \frac{2}{QE}\sqrt{\frac{I_{coll}^{dark}}{\Delta t}} + \frac{2C}{QE \cdot \Delta t} \approx \frac{2}{QE}\sqrt{\frac{I_{coll}^{dark}}{\Delta t}} \text{ for large } \Delta t. \tag{12}$$

If it is possible to extend the measuring time Δt without limits and if we have a constant flux of photons, it is always possible to comply with (12). This is where the ADC-unit and the dark current comes in as a limiting factor for Δt. Suppose it has a range R, and a resolution r, then we cannot detect more than $R*r$ electrons. With a dark current of I_{coll}^{dark} electrons*s^{-1} the maximum measuring time is $\Delta t_{max}=R*r/I_{coll}^{dark}$. This puts a bottom limit on the detectable photon flux ψ_{coll}^{light} leading to the detection limit

$$\psi_{coll}^{light} > \frac{2}{QE}\left(\frac{1}{\sqrt{R\cdot r}}+\frac{C}{R\cdot r}\right)I_{coll}^{dark} \approx \frac{2}{QE\cdot\sqrt{R\cdot r}}I_{coll}^{dark}. \tag{13}$$

Of course it is possible to extend the effective measuring time Δt to infinity by performing repetitive measurements each of duration Δt_{max}. Therefore, it is necessary to state a desired measuring time, and then calculate the detection limit for that time.

When we want to compare two systems, say system 1 and system 2, it is inviting to compare their photon flux detection limits (for large Δt):

$$\psi_{min,1} = \frac{2}{QE_1}\sqrt{\frac{I_{coll,1}^{dark}}{\Delta t}} \tag{14}$$

$$\psi_{min,2} = \frac{2}{QE_2}\sqrt{\frac{I_{coll,2}^{dark}}{\Delta t}}$$

Calculating their ratio yields

$$\frac{\psi_{min,1}}{\psi_{min,2}} = \frac{QE_2}{QE_1}\sqrt{\frac{I_{coll,1}^{dark}}{I_{coll,2}^{dark}}}, \tag{15}$$

which gives a quick impression of the relative qualities of the two systems at low photon fluxes.

2.4.1.2 Large photon fluxes

For photon fluxes much larger than $QE*I_{col}^{dark}$, we find for the signal-to-noise ratio sn^{-1}

$$sn^{-1} = \sqrt{QE\cdot\psi\cdot\Delta t} \tag{16}$$

Comparing two systems, we find with (16) for the ratio of their sn^{-1} ratios

$$\frac{(sn^{-1})_1}{(sn^{-1})_2} = \sqrt{\frac{QE_1}{QE_2}} \tag{17}$$

2.4.1.3 Data provided by the manufacturers

Some relevant data of the investigated systems is displayed in the Table 1. The numbers are based on data provided by the manufacturers[2]. The first row of the table provides information about the geometry of the considered systems. The equivalent times t_{eq} are the calculated

time it takes for the shot noise because of dark current to reach the amount of electrons specified.

System:	PDA RL1024S	PMT R376	CCD ST6-UV
Format (pixel field)	1024 * 1	1*1	375 * 242
Dark current per unit surface at -20°C	$1*10^{13}$ electr. $s^{-1}m^{-2}$	$2*10^{6}$ electr. $s^{-1}m^{-2}$	$2*10^{10}$electr. $s^{-1}m^{-2}$
Constant noise in electrons/readout	$1.5*10^{3}$ t_{eq} = 3.6 s.	-	25 t_{eq} = 48 s.
Pixel size	25μm * 2.5 mm	round $6.2*10^{-4}$ m^2	23 μm * 27 μm
Saturation charge per unit surface (electrons m^{-2})	$1.4*10^{15}$ electrons	-	$3.2*10^{14}$ electrons
ADC resolution nr. of electrons	1300 t_{eq} = 1.2 s.	-	6.7 t_{eq} = 0.5 s.

Table 1. Relevant data from data sheets systems.

Quantum efficiencies as specified by the manufacturers are depicted in Figure 4.

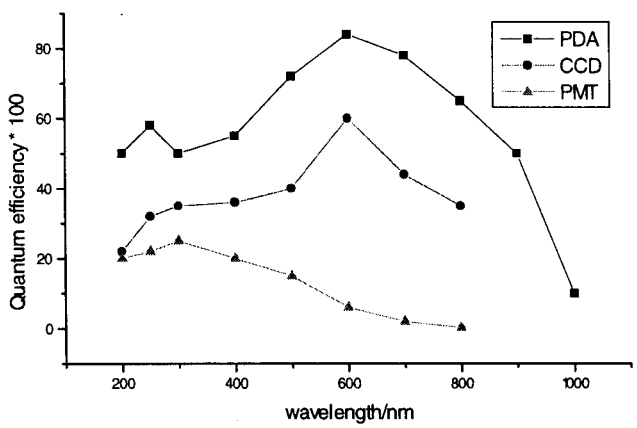

Figure 4. Quantum efficiencies as function of wavelength. The plots are based on data provided by the manufacturers.

2.4.1.4 Example

For this example we consider 1) 1 mm x 1 mm and 2) 0.1 mm x 0.352 mm illuminated area on each detector. We will assume that it is possible to select just the right amount of necessary pixels in case of the CCD and the PDA, but that we need to use the whole PMT-surface. Furthermore we do not want to measure for longer than 300 s.

Making use of equation (12) for the detection limits, equation (15) and (17) for the performance of the systems relative to that of the CCD and the system data provided in the last section, we find the following results for a wavelength of 600 nm and at -20°C:

Δt = 300 s	PDA RL1024S	PMT R376	CCD ST6-UV
Dark current (electrons s^{-1})	1×10^{7} / 3.5×10^{5}	1×10^{3} / 1×10^{3}	2×10^{4} / 704
Quantum efficiency at 600 nm	0.85	0.06	0.6
Photon flux detection limit ψ_{min} (s^{-1})	4.3×10^{2} / 80	54 / 54	27 / 5
$\psi_{min}/\psi_{min,CCD}$ (small photon fluxes)	16 / 16	2 / 11	1
sn^{-1}/sn_{CCD}^{-1} (large photon fluxes)	1.2 / 1.2	3.2 / 3.2	1

Table 2. Comparison for 1 mm² / 0.0352 mm² illuminated detector surface, a desired measure time of 300 s and wavelength 600 nm.

The comparison becomes more favorable for the CCD when the desired detector surface decreases, and for higher wavelengths. If the surface increases n-fold, the relative PMT photon detection limit falls with sqrt(n). The wavelength dependency of the relative photon detection limit becomes visible in Figure 5.

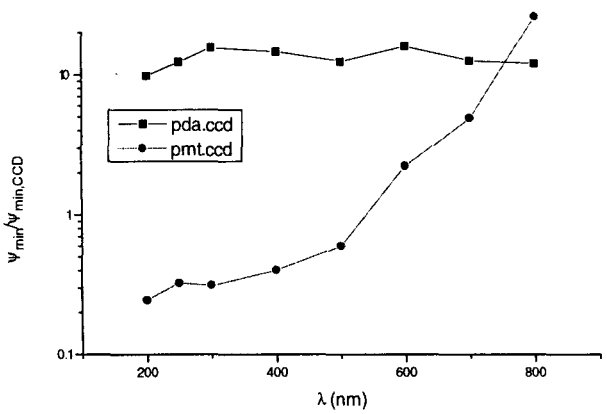

Figure 5. Relative detection limits. For lower wavelengths the PMT performance improves due to quantum efficiencies.

This figure illustrates the strong variation in spectral response of the PMT compared to both of the other systems.

2.4.2 Verification experiment

In order to verify the specifications of the PMT and the CCD claimed by the manufacturer, an experiment is done resulting in the ratio of the number of electrons collected with the CCD and with the PMT, when they are illuminated with the same amount of photons of the same wavelength.

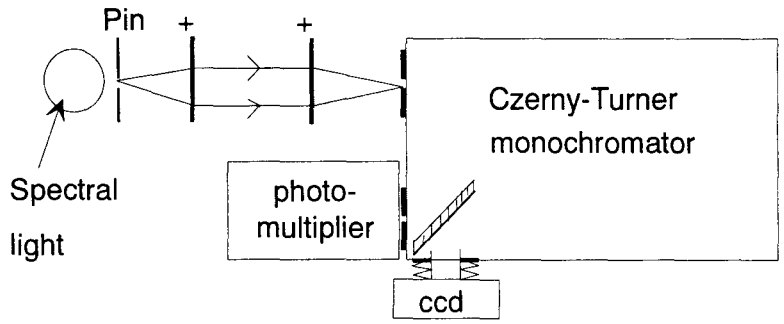

Figure 6. Setup of the experiment to compare the spectral response of the CCD with the PMT.

Both CCD and PMT are mounted at the exit of the monochromator, with a flat mirror it is possible to switch between them. The 25 μm entrance slit of the monochromator is illuminated with a light spot at the center of the slit. The spot was the one to one image of a 1 mm pinhole (Pin) covered with light diffusing tape, illuminated with spectral lamps.
In order to cover the spectral region of 200 - 800 nm, spectral lights containing Ar, Cd and Zn are used. In this region, 8 emission lines are selected strong enough to be in the large photon flux region.
The exit slit between the PMT and one of the exit of the monochromator has a width of 500 μm, allowing a full spectral line to enter the PMT. The PMT entrance window has a diameter of 28 mm and all of the slit heights are 19 mm. The dimensions of the CCD-array are 8.8 mm x 6.6 mm. The chosen combination of exit slit, PMT, CCD and pinhole ensures that there is an unlimited image of the spectral lines on the surfaces of the PMT and the CCD.

2.4.3 Result and discussion

The ratio of the number of counted electrons on the illuminated part of the CCD surface and the counted electrons from the PMT are plotted in Figure 7.

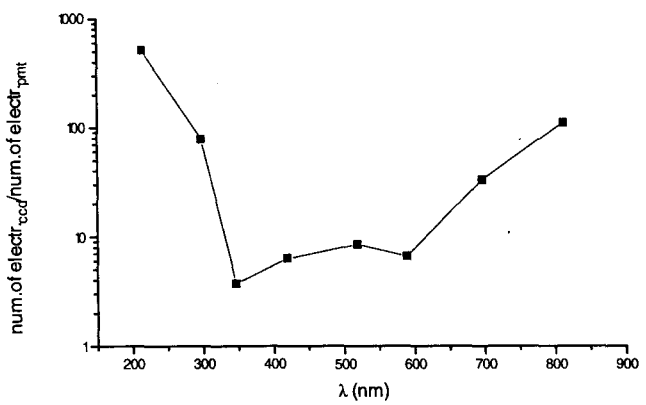

Figure 7. Ratios of collected electrons per unit time. The behavior under 350 nm is due to a limiting quartz window.

Remarkable is the behavior under 350 nm, where the CCD's sensitivity increases strongly compared to the PMT sensitivity. This is caused by a inferior quartz window between the exit of the monochromator and the PMT, closing of the PMT-chamber in order to prevent condensation on the cooled tube.
If we ignore this for a second, and calculate the quantum efficiencies of the CCD based on those specified by the PMT-manufacturer, we get the result depicted in Figure 8

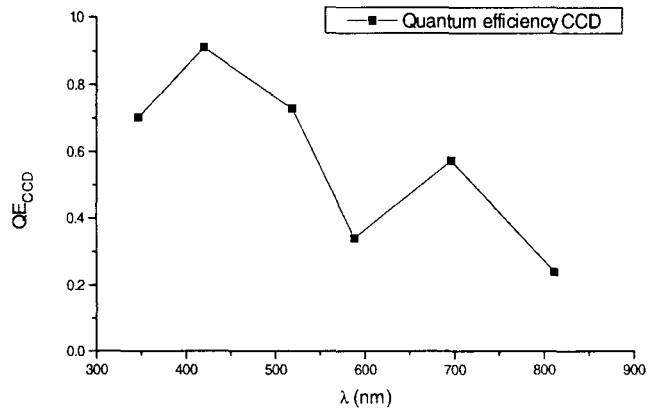

Figure 8. Quantum efficiencies of CCD calculated from the experiment and PMT specifications.

The absence of values of the QE_{CCD} for wavelengths lower than 350 nm is due to the effects of the quartz window, which also might affect the rest of the measured values, especially those at lower wavelengths. For QE's in the range of 350 to 500 nm, we find significantly higher values than specified by the CCD manufacturer. This means the SBIG CCD QE's are indeed higher than specified, or that the PMT QE's are over-estimated by Hamamatsu, or that the window closing the PMT chamber has an absorption coefficient $\kappa > 10\%$ over a large wavelength range of 200-500 nm.

2.4.4 Conclusions

Comparison of the three systems is a complex matter, depending very much on the experimental setup and the actual detection area used. The main reason for this complexity is the fact that that the CCD detection surface can be limited by the user, while the PMT surface is indivisible.

From comparison experiments of the CCD with the PMT, we can conclude that if the PMT quantum efficiencies are correct, and if the window closing the PMT chamber has an absorption coefficient below 10% for wavelengths higher than 350 nm, claims made by SBIG about the quantum efficiencies of their CCD-array are under-estimations of the real values.

If we assume a used detection surface of 1 mm^2 and a measuring time large enough to exceed system thresholds, than the photon detection limit of the CCD is a factor of two better than that of the PMT, and a factor of 16 better than that of the PDA. If we assume a used detection surface of 0.0352 mm^2 and a measuring time large enough to exceed system thresholds, than the photon detection limit of the CCD is a factor of 11 better than that of the PMT, and a factor of 16 better than that of the PDA.

For detection surfaces much larger than 1 mm^2 the detection limit of the PMT become smaller than that of the CCD. For detection surfaces much smaller than 1 mm^2 the detection limit of the CCD become smaller than that of the PMT.

For experimental conditions where the thresholds are relevant (short measuring times and low photon fluxes), the CCD detection limits can be up to 60 times better than those of the PDA. It depends on the minimum detector readout time and used detector surface whether the CCD is superior to the PMT or visa versa.

For the case of large photon fluxes we can conclude that the choice is governed by the quantum efficiencies of the systems at the chosen wavelength. The system with the largest quantum efficiency will have the best signal-to-noise ratio. In that case the PDA would be the best choice of detection system.

2.5 Detection limits McALI set-up

If we go back to the experimental setup used in ALI measurements Figure 1, a detection limit can be given based on the last paragraph. The assumptions are that the closed ICP is optically thin for the considered 600 nm emission line, it has no continuum radiation, it has a line of sight thickness of 6 mm, and there is no background radiation of any kind. Furthermore, the system thresholds do not play a role (long measuring times). Given the entrance slit width of 100 μm, the binned CCD pixels height of 0.352 mm and the plasma thickness of 6 mm, a pixel observes a plasma volume V of approximately 100 μm x 0.352 mm x 6 mm corresponding to $2.1 \times 10^{-10} m^3$. Furthermore, because of the solid angle, we only get to see a fraction $\Omega/4\pi$ of the emission equal to 6.3×10^{-4}.
If we do not want to measure longer than 300 s, and we estimate the transition frequency A of the line we look at $10^6 s^{-1}$, then we find with

$$n_{\min} \cdot A \cdot V \cdot \frac{\Omega}{4\pi} = \psi_{\min} \tag{18}$$

where ψ_{min} is the photon flux detection limit, and n_{min} the minimum detectable density of the emitting atom, the minimum detectable densities listed in Table 3.

	PDA RL1024S	PMT R376	CCD ST6-UV
n_{min} (m^{-3})	6×10^8	4×10^8	4×10^7

Table 3. Detection limits for the three detection systems, in case of a fictive plasma with no continuum radiation and without any other type of background radiation, and a used detector surface of 0.0352 mm² (see Table 2).

From this calculation it follows that under the specified circumstances, the McALI setup can detection excited atom densities to a minimum of 4×10^7 m^{-3}. These limits are at least a factor of 10 better than the detection limits of the PDA and PMT.

2.6 Conclusions regarding construction and implementation

A two dimensional CCD camera is successfully installed at the exit of a monochromator thereby constructing a Multi channel Absolute Line Intensity device. It makes the simultaneous determination of population densities at several positions in the plasma possible. It is computer operated, for this purpose a Pascal function library was written allowing easy access to the camera functions.
The first important advantage of McALI is the time-saving aspect. A similar measurements with a PMT would mean repeating the measurement at 25 positions, and for at least three wavelength per position to determine the emission line background. Measurements would then take at least 75 times longer.
The second important point is that for accurate determination of emission line background radiation, wavelength resolved information is indispensable, especially for the very widened emission lines (FWHM > 1 nm) close to ionization.
An other advantage is the fact that the data about the plasma is obtained in one instant, thereby eliminating uncertainties in the measurement due to long term plasma instabilities and measurement conditions reproducibility. Especially when profiles have to be post-processed with for example Abel-inversion, this can be very beneficial.

Furthermore, the detection limits achievable with the CCD in comparison with other detectors gets increasingly favorable for the CCD for increasing spatial resolution. The reason for this is the relatively low dark count of a CCD, resulting in relatively low shot noise numbers.

---

[2] Santa Barbara Instrument Group, 'CCD Camera Operating Manual for the Model ST-4X, ST-5 and ST-6'.

Santa Barbara Instrument Group, 'Universal CPU Command Structure', December 15, 1993.

EG&G Reticon, 'PDA data sheet S-series solid state line scanners 1024 elements'. Datasheets.

Hamamatsu, 'Head-On type Photomultipliers'. Datasheets.

3 Transition probability corrections by exploiting pLSE conditions.

3.1 Introduction

Absolute line emission intensity (ALI) spectroscopy can be a powerful technique to determine the important plasma parameters like electron density n_e and electron temperature T_e . Especially for the closed ICPs under investigation, n_e and T_e largely determine the atomic state population density, having a direct effect on light production. The procedure followed requires the determination of absolute population densities of a number of electronic states. These are the top levels of the dipole transitions causing the line emission we observe with this technique.
If the atomic state distribution for these levels is described by the Saha equation, we can use this equation to obtain n_e and T_e from these population densities. Because the validity of the Saha equation increases the closer the energy of the atomic state approaches the ionization energy of the atom, transition lines with a top energy level close to ionization energy are likely to provide the best determinations of n_e and T_e.
When obtaining n_e and T_e this way, transition probabilities A of the considered transitions should be known in order to calculate population densities from observed line emission. For the low energy part of the excitation space of Ar, these values are accurately known[1], but for this region significant deviations from Saha behavior might occur, making accurate determination of n_e and T_e impossible. However, for the part of excitation space where population behaves according to Saha, transition probabilities are poorly defined[1] with specified uncertainties reaching up to more than 50%.
Therefore, more accurate transition probabilities for the upper part of excitation space are needed. Transitions from this region are usually weak and heavily broadened, requiring sensitive and wavelength resolved emission detection to determine the total line emission. This makes the CCD array introduced in the last chapter a very suitable detection device.
In this chapter, 15 improved transition probabilities will be calculated from experiments on an *open* argon ICP with two diagnostical techniques: Thomson scattering (TS) yielding electron temperatures and ALI yielding atomic level populations.
The power of TS is the ability to accurately determine spatially resolved electron temperatures as well as spatially resolved electron densities in wall-less plasmas. However it is less suitable as diagnostic for closed ICPs because of significant laser light scattering on the plasma enclosure. The improved transition probabilities allow us to obtain more accurate values for n_e and T_e with ALI, a diagnostic that does not have this scattering problem.

3.2 Experimental

ALI and TS experiments are performed on an *open* atmospheric argon ICP with a RF generator frequency of 100 MHz. Power is coupled into the plasma using a coil consisting of two windings around the plasma torch. The RF generator power is 1.2 kW. The argon flow is 13 l/min.

Figure 1 shows the plasma torch with maximum inner diameter of 18 mm, and the definition of the used coordinates. The TS and ALI measurements are obtained at h = 7 mm Above Load Coil (ALC). Note that the plasma has cylindrical symmetry indicated by the horizontal dotted line in the figure.

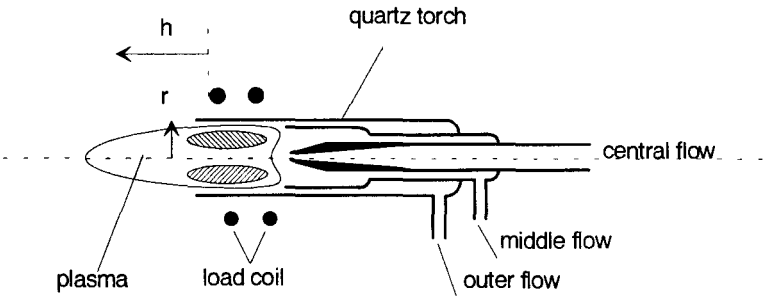

Figure 1. The plasma torch. The h-coordinate is parallel to the axis of symmetry drawn as the horizontal dotted line in this picture. The plane h = 0 touches the top of the load coil, at the point the furthest away from the generator. In the laboratory situation, the h-axis correspond to height. Experiments were done at h = 7 mm ALC.

Figure 2 depicts the ALI setup. It consists of a 1 m monochromator with 2d-CCD array placed in its focal plane. For a detailed description of the setup see section 2.3. An additional image rotator is placed into the optical system to image a horizontal plasma section at h = 7 mm ALC onto the vertical entrance slit of the monochromator.

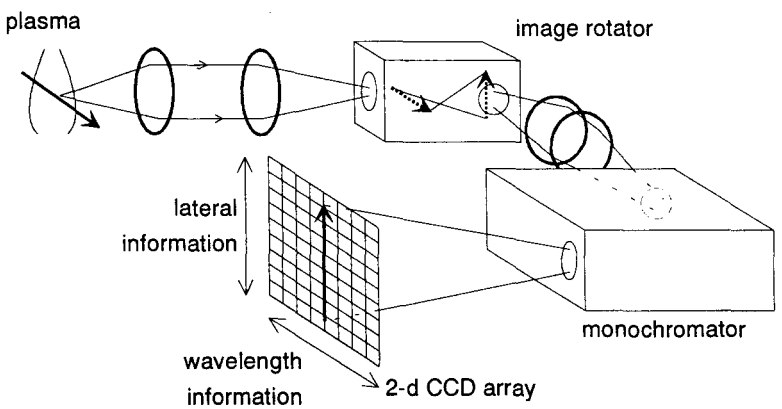

Figure 2. ALI setup. The image rotator is placed into the optical system to image a horizontal plasma section at h = 7 mm ALC onto the vertical entrance slit of the monochromator. The monochromator causes dispersion in horizontal direction. Information corresponding with lateral plasma information is projected vertically on the CCD-array.

Since the height of the CCD plane is 8.8 mm, it is possible to investigate one half of the plasma at once. The entrance slit width is 100 μm.

The CCD camera is operated in mode 3, with 10 fold software binning, thereby providing spatially resolved information about an emission line at 25 positions in one half of the plasma at once. This information consists of a wavelength interval surrounding the emission line. For every position, the emission line profile is decreased with background and wavelength integrated. The resulting 25 emission values are Abel inverted[2] to obtain local values for the line emissivity as function of radius. Abel inversion is necessary to convert the 'line of sight' data to local radial resolved data. It introduces additional uncertainties in the data, especially in the center of the plasma (r = 0). For this reason, Abel inverted data is discarded for r < 3.9 mm. The method of ALI for determination of the absolute population density of an initial atomic state of an transition is explained in section 2.3.1.2.

The TS diagnostic consists of a pulsed Nd:YAG laser, and the detection branch. For a complete description see de Regt et al[3]. In short, the principle of Thomson scattering is scattering of photons on free electrons. The Doppler effect causes the wavelength spectrum

of the scattered photons to have a *corrected Gaussian* shape. An example of a Thomson scattering spectrum is depicted in Figure 3.

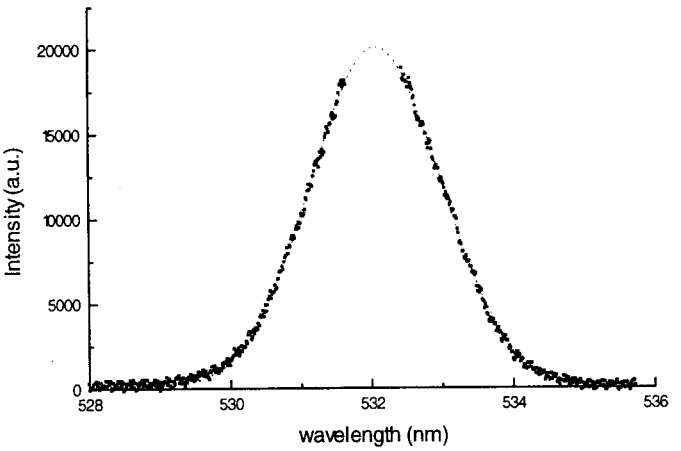

Figure 3. A typical Thomson scattering spectrum for $T_e = 8925 \pm 150$ K with a fitted *corrected Gauss* profile.

In first order, we can state that the shape is Gaussian, and the relation between electron temperature T_e and Gauss width is given by

$$T_e \propto (\Delta\lambda_G)^2, \tag{1}$$

with $\Delta\lambda_G$ the 1/e full Gauss width. For high electron densities, collective scattering takes place, i.e. scattering on a group of electrons. This becomes a relevant effect in our atmospheric plasma with electron densities n_e of order 10^{21}m^{-3} and $T_e \approx 9000$ K. This causes the spectrum to have a *corrected Gaussian* shape.

From spectra at several positions electron temperatures are determined[4], and a radial electron temperature profile is constructed. Temperatures at positions not measured in the region r = 3.9 mm to r = 6.7 mm are calculated with a interpolation polynomial of order 6. Figure 4 shows the electron temperature profile determined with TS.

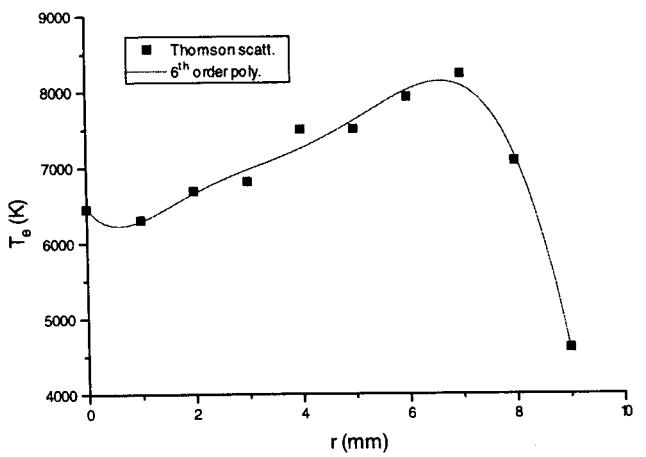

Figure 4. TS electron temperature profile at 7 mm ALC, with polynomial fit of order 6. Electron temperatures are corrected for collective scattering.

3.3 Method of determining transition probabilities

The central assumption in the procedure to determine transition probabilities is that of validity of the Saha equation for the top states involved in the transitions. In other words, the top states of the transitions are in partieel Local Saha Equilibrium (pLSE), and the Saha equation is the atomic state distribution function (ASDF). This implies that for these states the ionization-recombination reaction

$$A^+ + e + e \Leftrightarrow A_p^0 + e \tag{2}$$

is dominant. Here A^+ denotes the ion, e the electron and A^0_p the neutral particle with internal energy E_p .
For plasmas with electron densities n_e of order 10^{21} m^{-3} and electron temperatures of T_e>7000K, states with energy levels closer than 0.6 eV from ionization will certainly be populated according to Saha[5]. If T_e, n_e and the ion density n_i are known, the population density of an atomic state p at energy ΔE_p from the ionization energy E_{ion} is described by the Saha equation

$$\eta_p^S = \frac{n_i n_e}{2g_i} \frac{h^3}{(2\pi m_e kT_e)^{3/2}} \exp\left(\frac{\Delta E_p}{kT_e}\right). \tag{3}$$

In this equation is $\eta_p{}^S$ the density n_p of a state p per statistical weight g_p, g_i the statistical weight of the ion ground level, $\Delta E_p = E_{ion} - E_p$ the energy difference between ionization energy and the energy of state p, h Planck's constant, k the Boltzmann constant and m_e the electron mass. This equation can also be written as

$$\eta_p^S = \eta_\infty^S \exp\left(\frac{\Delta E_p}{kT_e}\right), \tag{4}$$

with η_∞ the imaginary density at ionization energy

$$\eta_\infty^S = \frac{n_i n_e}{2g_i} \frac{h^3}{(2\pi m_e kT_e)^{3/2}}. \tag{5}$$

On the other hand, η_p, can be expressed by

$$\eta_p = \frac{4\pi j_p}{g_p \cdot A_{pq} h\nu}, \tag{6}$$

where $h\nu$ is the photon energy, and A_{pq} the transition probability of the emission line. For three carefully selected argon transitions well in the pLSE region, transition probabilities are relatively well known with accuracies of ±25%. These transitions are 6d - 4p, 5d' - 4p, and 7s - 4p with respective emission wavelengths of 516.2 nm, 518.8 nm and 588.9 nm. ALI experiments at those wavelengths yield the respective emissivities j_p, leading to initial level densities with equation (6).

With equation (4) three corresponding values of η_∞ are determined, hereby making use of T_e from Thomson scattering. These three values are averaged to yield a more accurate value of η_∞^S with an uncertainty of ±14%.
At this point it is possible to calculate transition probabilities for other transitions. Combining equations (4) and (6), for ΔE_p < 0.6 eV and having j_p determined from ALI experiments, A_{pq} can be calculated according to

$$A_{pq} = \frac{4\pi j_{pq}}{h\nu g_p \eta_\infty^S} \exp\left(-\frac{\Delta E_p}{kT_e}\right) \tag{7}$$

For a visualization of the method it can be noted that the points in zone III of Figure 5 scattered around the line with a slope determined by T_e and an offset determined by the densities of the three reference densities marked by 'X', are 'forced' upon that line by changing their transition probabilities.

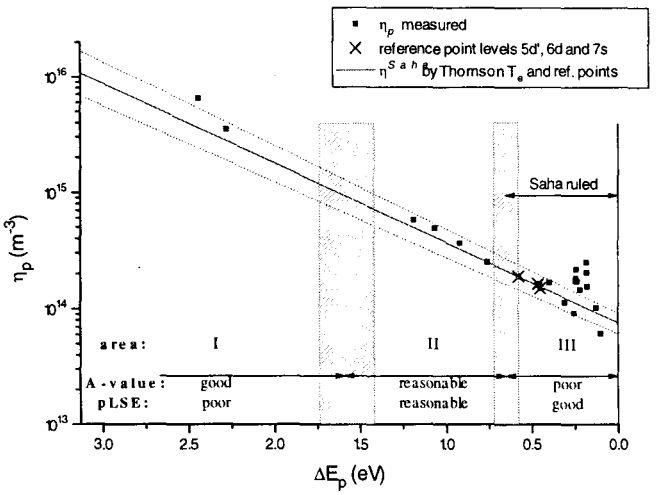

Figure 5. Logarithmic plot of the ASDF at r = 6 mm at h = 7 mm ALC. In zone III, we assume population behavior according to Saha. These levels are included in our transition probability correction method. Note the large scattering in this area. The solid central line is based on T_e determined with Thomson scattering, and η_∞ defined by the population densities of the states indicated with the crosses; these states have transition probabilities with uncertainties within 25%. The dotted band indicates the total uncertainties. The reference levels 5d', 6d and 7s correspond to 518.8 nm, 516.2 nm and 588.9 nm respectively and are marked by 'X'.

The figure furthermore shows that transition top level population densities in zone I are, in spite of their accurately known transition probabilities (< 10%), over-populated compared to Saha population. Zone II is a transition zone with reasonable Saha behavior, and reasonably well known transition probabilities.

3.4 Results

The method for determination of transition probabilities is applied for 15 argon transitions with initial states close to the ionization level, ΔE_p < 0.6 eV. Per transition the method is repeated for nine positions between r = 3.9 mm and r = 6.7 mm, and the resulting nine A_{pq} - values per transition are displayed in Figure 6.

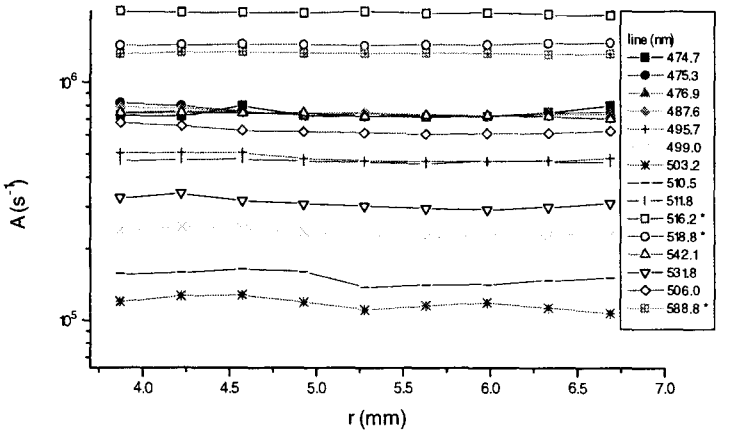

Figure 6. Calculated transition probabilities at nine plasma positions between r = 3.9 mm and r = 6.7 mm. As should be the case, the dependency of calculated transition probabilities on position is neglectable within the specified uncertainties. The transitions indicated with a '*' are the reference transitions.

To derive A_p^{new}, these 9 values per transition are averaged, thereby further reducing random errors in A_{pq} due to random errors in η_∞, T_e and j_{pq}. The results are listed in Table 1. Note that new transition probability values fall within the specified margins of uncertainty of the old values. The uncertainties in the corrected transition probability A_p^{new} are σ_A= 20%. These uncertainties are expressed in Figure 5 by the outermost dotted lines.

λ (nm)	I_p (eV)	E_p (cm^{-1})	A^{old} (10^5 s^{-1})	$(\Delta A/A)^{old}$	A^{new} (10^5 s^{-1})
474.7	0.242	125163	3.70	> 50 %	7.44
475.3	0.245	125136	4.70	> 50 %	7.53
476.9	0.254	125067	9.00	50 %	7.40
487.6	0.311	124603	8.10	50 %	7.46
495.7	0.183	125631	1.90	> 50 %	4.83
499.0	0.181	125651	1.10	> 50 %	2.33
503.2	0.221	125329	0.85	> 50 %	1.17
506.0	0.234	125220	3.90	> 50 %	6.29
510.5	0.179	125671	0.91	> 50 %	1.51
511.8	0.243	125149	2.80	> 50 %	4.67
516.2 *	0.452	123467	20.00	25 %	19.40
518.8 *	0.464	123373	13.80	25 %	14.00
531.8	0.127	126090	2.70	> 50 %	3.11
542.1	0.398	123902	6.20	50 %	7.33
588.9 *	0.580	122440	13.40	25 %	13.30

Table 1. New transition probabilities, calculated from Thomson scattering electron temperatures and population densities determined with ALI. The new listed values are averages of transition probabilities determined at nine positions in the plasma in the region r = 3.9 mm .. 6.7 mm. Old transition probabilities are taken from [1]. Note that the new values of the transition probabilities fall within the specified margins of error of the old values.

3.5 Discussion

In the applied method for determining new transition probabilities A_p^{new}, η_∞ is calculated from ALI experiments, and T_e from TS. The final uncertainty in A_p^{new} is primarily caused by uncertainties in the transition probabilities of the three reference transitions. This causes a

systematic uncertainty in η_∞ of 14%. The second source of systematic errors is caused by Abel inversion, and is estimated at 5%. Note that these uncertainties cannot be reduced by averaging. Remaining sources of uncertainties in A_p^{new} are random uncertainties in T_e of 5%, and ALI photon detection random uncertainties of about 0.5%.
The applied method combines three measured population densities to calculate η_∞ in order to improve uncertainties, but can be extended to more than three transitions. The more transitions are involved, the more the resulting specified error will approximate the systematic errors, which are mainly caused by Abel inversion in these experiments.

An interesting verification of the new A-values can be given by examining the ASDF when it is reconstructed with new A-values and comparing it to a construction based on the old values, of which zone III of Figure 5 is an example. We expect a reduced scattering for all positions in the plasma. This is exactly what Figure 7 shows.

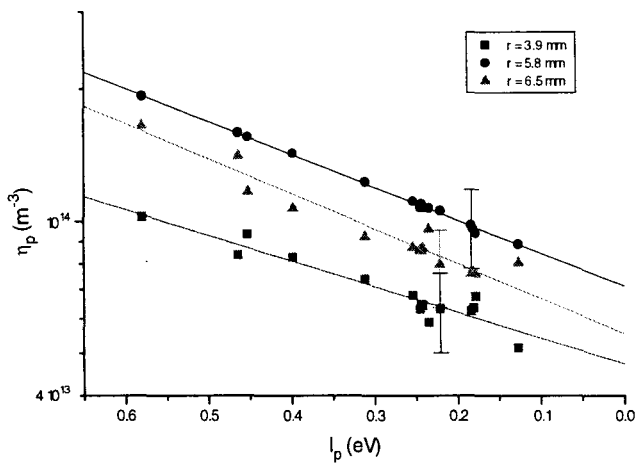

Figure 7. Saha plots based on ALI measurements processed with new transition probabilities. At three positions in the plasma, we observe scattering around a Saha line entirely within the specified margins of uncertainty. A dramatic improvement has taken place if we compare this scatter behavior with a formerly typical behavior of the points in zone III of Figure 5.

Within the specified margins of uncertainty, all level populations are on a Saha line, and the reduction in scattering behavior is remarkable indeed if we compare this to zone III of Figure 5.

3.6 Conclusions

A combination of ALI and TS can be used to determine transition probabilities of transitions with initial levels close to ionization and atomic state populations described by Saha.
Transition probability values and their uncertainties of 15 argon emission lines with initial states closer than 0.6 eV (4669.9 cm^{-1}) from the ionization energy of 15.76 eV (127109.9 cm^{-1}) have been determined successfully. Uncertainties of in many cases more than 50% have been reduced to 20%.

[1] W.L.Wiese, M.W.Smith, B.M.Glennon. Atomic Transition Probabilities Volume I and II. Institute for Basic Standards, National Bureau of Standards, Washington D.C.
[2] M.C.M. van de Sanden, 'The expanding plasma jet: experiments and model', Thesis 1991.

[3] J.M. de Regt, F.P.J. de Groote, J.A.M. van der Mullen, D.C. Schram, 'Thomson scattering experiments on a 100 Mhz inductively coupled plasma calibrated by Raman scattering', Review of Scientific Instruments 66 (3228), 1995.

[4] F.P.J. de Groote, ' Diagnostic tools for atmospheric plasmas compared', afstudeerverslag VDF-NT 95-27.

[5] J.M. De Regt, R.D.Tas, J.A.M. van der Mullen and D.C. Schram, 'Determination of transition probabilities for argon using Thomson scattering experiments on an inductively coupled plasma', submitted to Journ.Quant.Radiat.Transf.

4 The Closed argon ICP Mapped

4.1 Introduction

Inductively coupled plasmas (ICP) are widely used in diagnostical tools, and as stable plasma sources in more fundamental plasma research. Also the application of high pressure closed ICPs as light source has become a topic of interest because of the high light production efficiencies, and long lifetimes because of absence of electrodes-plasma contact.
In order to be able to improve our understanding of high pressure ICPs, fundamental research is carried out on closed argon ICPs, focusing on determination of spatially resolved heavy particle temperatures, electron temperatures and electron densities. These quantities govern the occupation of atomic states, which is important information regarding light production.
All measurements in this report are performed on closed argon inductively coupled plasmas. The eventual light source will very likely not be filled with argon, but because of our expertise regarding this gas, and in order to compare closed ICPs with other plasmas available here, it was decided to initially use argon.
This chapter will briefly describe the applied diagnostics, and their advantages and shortcomings in the context of our plasmas. It will furthermore present the results of measurements performed with the above techniques. Plasma behavior as function of filling pressure and plasma powerwill be examinated and these results will be discussed.

4.2 The plasma source

All of the investigated plasmas are created inside an cylindrical quartz vessel with an inner diameter of 18 mm and an inner height of 8 mm. The thickness of the wall is 1 mm. The opposing cylinder sides are optically flat for observation purposes. Power is supplied to the plasma by means of induction, and for this purpose a coil consisting of three turns surrounds the vessel, as depicted in Figure 1.

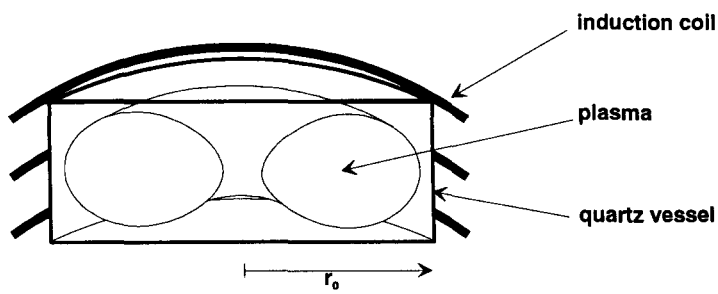

Figure 1. Cross section of the plasma vessel and the primary coil consisting of three windings surrounding the plasma vessel.

Power is supplied by a Dresser MPG 1315 RF power generator, at an operating frequency of 13.56 MHz. The output impedance of the generator is matched to the plasma-coil system impedance by a capacitor matching network.

The amount of power coupled into the plasma is determined by measuring the amount of forward and backward power to the matching network, and by measuring the current through the coil. A Rohde & Schwarz ZVP vector analyzer and a HP 438A power meter in combination with a HP 8481H power sensor are used for this purpose respectively. These devices are connected to a PC performing the calculations and supplying display facility. Figure 2 shows the setup as far as the RF equipment is concerned.

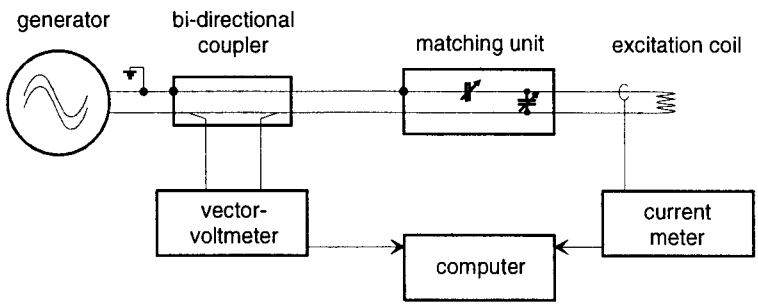

Figure 2. Sketch of the RF setup aimed at matching the generator and the plasma/excitation coil impedance's, and controlling the amount of plasma power.

All vessels used for this report are filled with argon, with filling pressure 10, 50 and 100 mbar at room temperature corresponding to argon neutral densities of 2.5×10^{23}, 1.2×10^{24}, and 2.5×10^{24} argon particles per m^3 respectively. A fourth vessel has a filling pressure of 50 mbar, with 0.025 volume % H_2 at filling time. After operating under plasma conditions for twenty minutes, the original amount of H_2 was reduced by outwards diffusion to a non detectable level.
A typical plasma operation power is 100 W, and for a 100 mbar vessel this corresponds with a coil current of 14.5 A. For the measurements in this report, plasma powers of 50, 75, 100 and 125 W are used. The plasma is ignited with a Tesla sparker.

4.3 Diagnostics

The diagnostical techniques applied in this project are 1) absolute line emission intensities (ALI), 2) line emission intensities during power interruption (LIPI), 3) Thomson scattering (TS), 4) diode laser absorption (DLA). An attempt was made to apply a H_β broadening technique (HB), but this proved to be less suitable because of quickly escaping hydrogen by outwards diffusion through the quartz walls of the plasma vessels
All diagnostic branches are computer operated, and results from measurements are immediately fed back to the computer.

4.3.1 Absolute line emission intensities (ALI)

ALI enables us to determine the absolute population density of an initial state of an atomic transition. If this is done for a number of transitions with varying energy distances of the initial level to ionization level (ΔE_p,), the results can be plotted in a so called Saha (Boltzmann) plot like Figure 3.

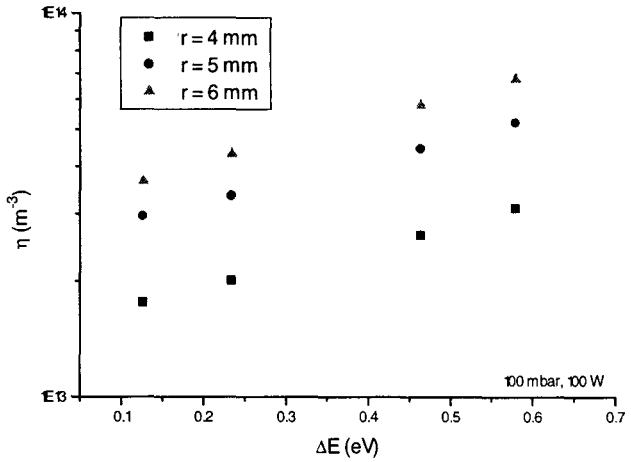

Figure 3. Saha plots from 100 mbar 100 W emission measurement at 3 positions in the plasma. The 4 emission lines used are 588.9 nm, 518.8 nm, 506.0 nm and 531.8 nm, all obeying pLSE.

The Saha equation can be written as

$$\eta_p^S = \eta_\infty^S \exp\left(\frac{\Delta E_p}{kT_e}\right) \tag{1}$$

with $$\eta_\infty^S = (n_+/g_+)(n_e/g_e)\left(\frac{h^2}{2\pi m_e kT_e}\right)^{\frac{3}{2}}, \tag{2}$$

and $$\eta_p = \frac{n_p}{g_p}, \tag{3}$$

the density of level p per statistical weight.
Dividing equation (1) by η_∞, and taking the natural logarithm of both sides yields

$$\ln\left(\frac{\eta_p^S}{\eta_\infty^S}\right) = \left(\frac{1}{kT_e}\right)\Delta E_p\,, \tag{4}$$

which shows that the slope of a linear fit through a scatter in a logarithmic plot as the one in Figure 3 corresponds to $1/(kT_e)$, and the offset at ΔE_p=0 equals η_∞. From equation (2) the product n_+n_e then can be calculated since T_e is known. Under the assumption that there is no multiply ionized argon atoms in the plasma, the electron density equals the ion density, and therefore n_e is known.
This method of determination of T_e and n_e can only be applied if the atomic states involved are populated according to Saha. In [4] it is shown that under present plasma conditions, for states not further away from ionization than 0.8 eV this is to be expected. The transitions used in this investigation are 588.9 nm, 518.8 nm, 506.0 nm and 531.8 nm. The initial states of these transitions are all closer to ionization than 0.6 eV, therefore obeying Saha population. The transition frequencies necessary to calculate the population densities from the absolute amount of line emission, are the ones determined in section 3.
Values of T_e yielding from these experiments should be interpreted with some care. Figure 4 shows the uncertainties in T_e values resulting from ALI experiments on the four transitions. Uncertainties in T_e increase with increasing T_e values, because the Saha plot slope decreases for increasing T_e values.

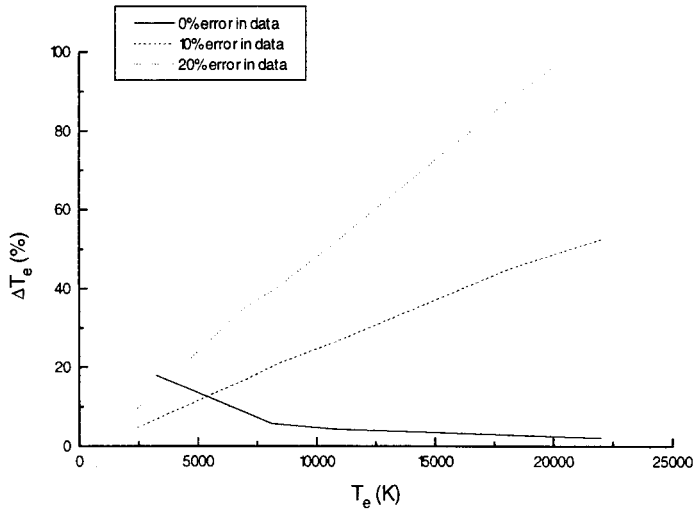

Figure 4. Uncertainties in T_e values resulting from ALI experiments on the four transitions 588.9 nm, 518.8 nm, 506.0 nm and 531.8 nm. The error in data percentage indicates the standard deviation in the (measured) level population of the top level of the transition. Uncertainties in T_e increase with increasing T_e values because of the decreasing slope in the Saha plot . The maximum error margins in the transition probabilities of section 3 are 20%, but it is found that 10% is a more reasonable estimation to work with.

The experimental setup used for ALI is identical to the one described in section 2.3.

4.3.2 Line emission during plasma power interruption (LIPI)

LIPI is based on the assumption that when plasma power is interrupted, electrons quickly cool to heavy particle temperature (typical time scale 1 μs), and relatively slowly recombine (time scale 100 μs).
A jump in line emission can be observed when the plasma power is interrupted. This jump is a result of the adaptation of the atomic state distribution to the new electron temperature. An example of this jump is shown in Figure 5.

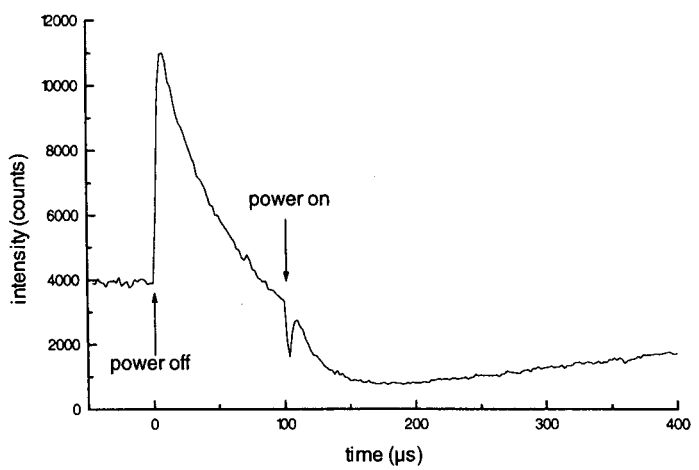

Figure 5. Example of an emission jump of the 588.9 nm Ar line during power interruption of the plasma with 100 mbar filling pressure and 100 W plasma power.

Knowing that line emission is proportional to the population density of the top level of the transition the magnitude of the jump can be calculated under the condition that the population of the initial energy level remains populated according to Saha, and that n_e is constant during

the cooling period. By dividing the Saha* equation ('*' indicating during power interruption) by the Saha equation before power interruption follows an expression for the jump [1].

$$\ln\left(\frac{\eta_p^{S*}}{\eta_p^{S}}\right)=\frac{3}{2}\ln\gamma+\frac{\Delta E_p}{kT_e}(\gamma-1) \qquad (5)$$

with η_p^S the population per statistical weight of the top level p of the transition before power interruption in m^{-3}, and η_p^{S*} the same quantity after cooling down of the electrons. γ is defined as the ratio of the electron temperature T_e before interruption and the temperature T_e^* after cooling of the electrons. ΔE_p is the energy distance of the top level of the transition to the ionization energy.
It follows from (5) that a measurement of the jump for several emission lines, and extrapolation to ΔE_p=0, yields γ. An example of such a measurement is displayed in Figure 6.

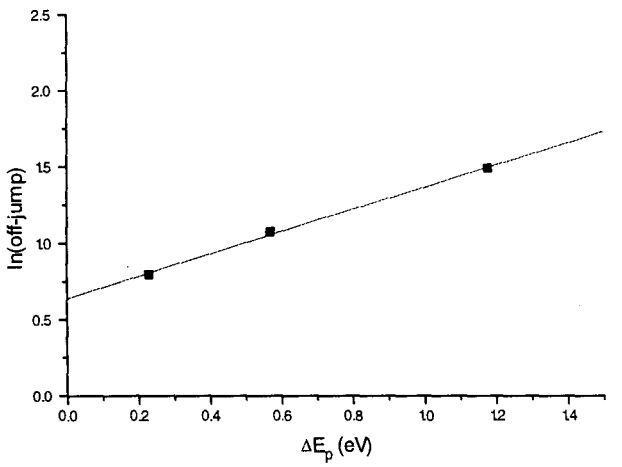

Figure 6. The emissivity jump for three transitions 588.9 nm, 518.8 nm, 506.0 nm. γ Is derived from the intersection with the $\Delta E_p = 0$ axis.

T_e^* can be calculated if T_e is known from a different experiment, for example ALI. Recently it has been shown[2] that T_e^* does not equal the heavy particle temperature T_h, but is significantly higher because of three particle recombination energy heating the electrons. T_e^* can therefore be regarded an upper limit T_h.
The LIPI experimental setup is depicted in Figure 7. It consists of a Hamamatsu R376 photomultiplier connected to a 1 meter B&M monochromator with an 1200 lines per mm grating. A small section of the plasma selected by the 1 mm pinhole is imaged onto the entrance slit (100 μm) of the monochromator. The selected spectral line is projected onto the exit slit (0.5 mm) of the monochromator. The power generator providing RF power to sustain the plasma, is switched off by the computer. For the next few hundred micro seconds, plasma line emission is observed by the photomultiplier, converted to a digital signal by the amplifier/discriminator, registered by the multi channel scaler and fed back to the computer[3].

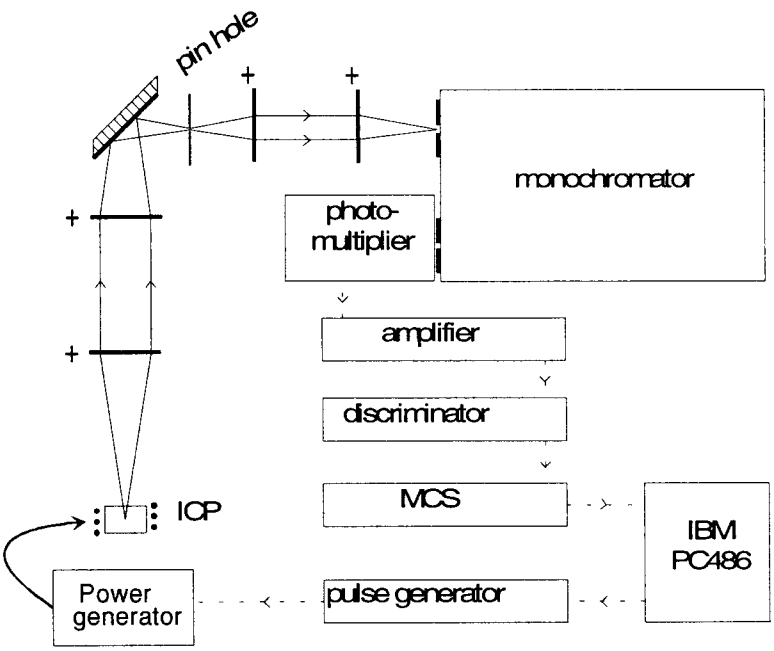

Figure 7. The LIPI experimental setup. The power generator providing RF power to sustain the plasma, is switched off by the computer. For the next few hundred micro seconds, plasma line emission is observed by the photomultiplier, converted to a digital signal by the amplifier/discriminator, registered by the multi channel scaler (MCS) and fed back to the computer.

The time behavior of five argon emission lines* are observed during a generator power interruption of 80 μs. The 696.5 nm line was later excluded because of the relatively large energy distance to ionization, causing its population to significantly deviate from Saha. When we strictly apply the pLSE condition of 0.8 eV[4], the 419.8 nm transition should also have been excluded.

4.3.3 Diode Laser absorption (DLA)

DLA is based on the ability to determine the shape of an absorption line profile of the $4s^3P_2$-$4p^3D_3$ argon transition corresponding to 811.531 nm (Figure 8), using a wavelength-tunable diode laser.

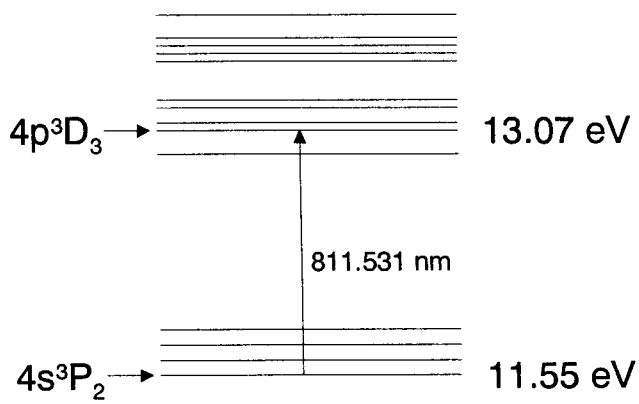

Figure 8. 4s-4p absorption in the argon atomic system. The corresponding wavelength is 811.531 nm. The $4s^3P_2$-$3p^1S_0$ (ground state) transition is forbidden, making this the $4s^3P_2$ state metastable.

* 696.5 nm, ΔE=2.44 eV; 419.8 nm, ΔE=1.265 eV; 588.9 nm, ΔE=0.575 eV; 518.8 nm, ΔE=0.455 eV; 506.0 nm, ΔE=0.235 eV.

The shape of the absorption profile will generally closely resemble a Voigt profile, i.e. a convolution of a Gaussian and a Lorentzian profile. An example can be seen in Figure 9.

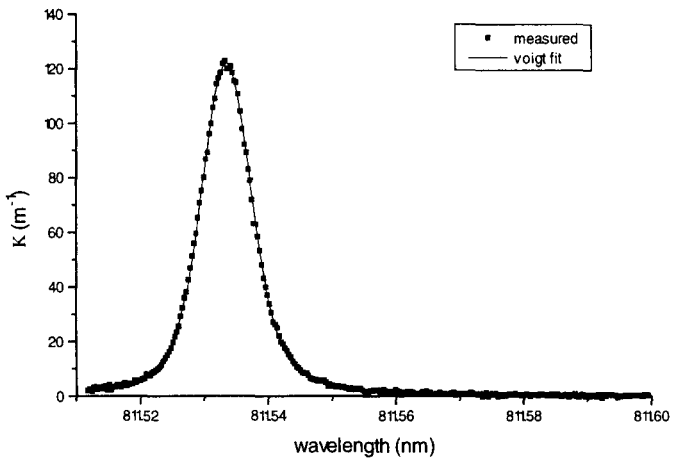

Figure 9. An example of an absorption line profile with a Voigt fit (full line). The Voigt fit is uniquely formed by the 1/e Gauss width, the FWHM Lorentz width, the place of the top, the height of the top and the offset of the profile. The first two parameters determine T_h and n_e respectively, the surface under the profile determines the 4s population density n_{4s}.

Deconvolution will yield[5] the Gauss width $\Delta\lambda_G$, the Lorentz width $\Delta\lambda_L$ and the surface S under the profile. These three parameters are unique for a given Voigt profile, and under a number of conditions[5] reveal the heavy particle temperature T_h , the electron density n_e and the population n_q of the lower state involved in the transition according to

$$T_h \propto (\Delta\lambda_G)^2 \tag{6}$$

$$n_e \propto \Delta\lambda_L \tag{7}$$

$$n_q \propto S \tag{8}$$

were we assume that the gaussian part of the Voigt profile is only due to Doppler broadening, and heavy particle temperatures are the same for all heavy particles, regardless of their state of excitation.

Equation (7) is only valid if Stark broadening is the only contribution to the Lorentzian component, which is generally not the case[5]. The second broadening mechanism leading to contribution to the Lorentzian component of the Voigt profile is Van der Waals broadening, estimated at 2.5 pm, 1.2 pm and 1 pm for 100 mbar, 50 mbar and 10 mbar filling pressures respectively. Resonance broadening also contributes to the Lorentzian component, but can be ignored because the $4s^3P_2$ level is metastable. The estimations of these contributions to the Lorentz width is based on [6]. These estimations should be compared to a Stark width of 1-20 pm for a typical n_e range of $10^{20}m^{-3}$ to $10^{21}m^{-3}$. Especially for lower values of n_e, Van der Waals broadening may contribute significantly to the Lorentzian component of the Voigt profile.

Figure 10 shows the experimental setup for the diode laser experiment. An detailed description of the setup can be found in [5]. The key element in this setup is a Sharp LT016MD0 diode laser with a wavelength corresponding to the $4s^3P_2$ -> $4p^3D_3$ argon transition, 811.531 nm.

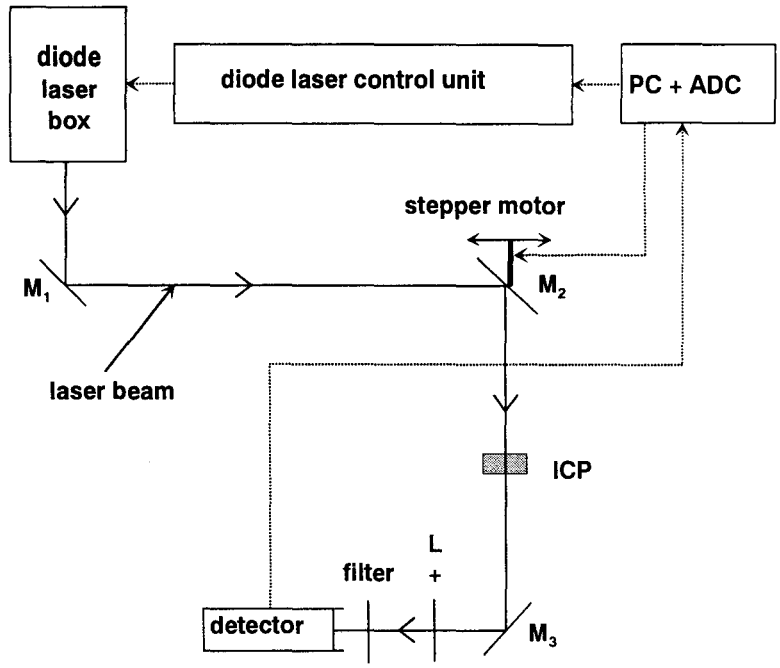

Figure 10. The tunable diode laser setup. Diode laser current and temperature are computer controlled making it possible to change the laser wavelength. A computer controlled stepper motor enables radial plasma scans. The red filter in front of the detector decreases the amount of detected plasma emission.

The temperature of the diode laser is controlled with a Peltier element to within 1 mK stability. A change of diode laser current, causes a change in the laser wavelength (6 pm/mA). This feature is used to make wavelength scans, with wavelength steps of 0.3 pm. Measuring the fraction of laser power absorbed in the plasma as function of wavelength yields the shape of the absorption line. By means of the movable mirror M_2 it is possible to make a radial scan of the plasma.

4.3.4 Thomson scattering (TS)

In short, the principle of Thomson scattering is scattering of photons on free electrons. The Thomson scattering branch consists of a high power pulsed Nd:Yag laser, and a optical detection branch perpendicular to the laser beam. Plasma continuum emission is minimized by only amplifying the detected Thomson signal during a small interval of time when the laser fires. For a complete description of the experimental set up see de Regt et al[7].
A number of extra measures is needed to minimize the vast amount of the stray light caused by scattering on the quartz vessel walls. A polarizing filter is placed in the detection branch, since the Thomson scattered signal is polarized and the stray light not, resulting in an increased signal-to-noise ratio. To minimize the 'cone of sight' in order to further reduce stray light, extra diaphragms are added. Finally, an additional reference measurement is performed with plasma off.

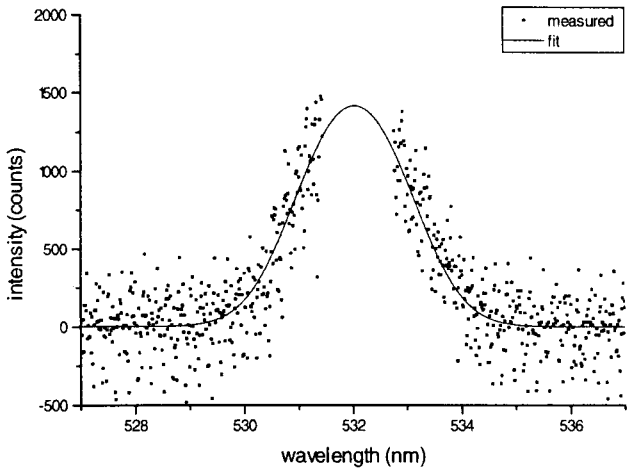

Figure 11. Thomson scattering spectrum at r = 6 mm, p_0 = 100 mbar and P = 100 W after correction for scattering on the vessel walls. The full line is the best corrected Gauss fit corresponding to T_e = 9300K ± 600K.

This spectrum is subtracted from the normal Thomson spectrum with plasma on. The resulting spectrum is shown in Figure 11.

4.3.5 H_β emission line broadening

By studying the shape of the Balmer H_β line (486.13 nm), it is possible to determine the electron density n_e.

Two processes are mainly responsible for broadening of the H_β line: Thermal broadening due to the Doppler effect and Stark broadening due to interaction of electrons with the hydrogen particles. Thermal broadening leads to a Gaussian line shape, Stark broadening to a Lorentzian. In a similar way as with diode laser absorption, the resulting line profile is Voigt-shaped. If the Stark width (FWHM) $\Delta\lambda_L$ >> Gauss width *(1/e)* $\Delta\lambda_G$, which is normally the case, the H_β line shape will be Lorentzian, and the electron density can be calculated using[8]

$$n_e = 7.124 \cdot 10^{20} \left(\frac{\Delta\lambda_L}{\Delta\alpha_{1/2}} \right)^{\frac{3}{2}} \qquad (9)$$

with $\Delta\alpha_{1/2}$ the theoretical width of the reduced wavelength α (FWHM) in Åcm/statvolt, as calculated and published by for example Griem[9], and compared with experimental values by for example Helbig et al[10]

The H_β measurements were performed with the same detector branch as the ALI experiments of section 2.3, but with the CCD in the plane of maximum wavelength resolution and with a 25 μm entrance slit.

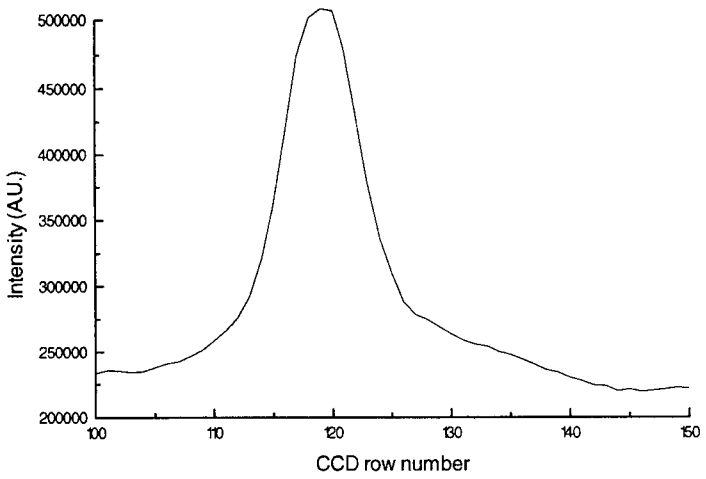

Figure 12. A H_β profile visible at 486.13 nm in an open 1.2 kW flowing argon ICP. One CCD row corresponds to a 20 pm wavelength interval.

In the presents of atomic hydrogen, a H_β profile typically looks like the one in Figure 12.

4.4 Results

4.4.1 Thomson scattering

Because of the difficulty of the experiment, Thomson scattering is only done for one position in the 100 mbar vessel, at a plasma power of 100 W. The resulting electron temperature is 9300K ± 600K. This temperature has been corrected for collective scattering[2].
Also experiments on a different plasma[8], the open argon ICP of section 3, shows a good agreement between ALI and TS electron temperatures.

4.4.2 H_β emission line broadening

After having warmed up the equipment for a few minutes, no H_β emission could be detected at 486.13 nm. Verification with an open argon ICP yielded Figure 13.

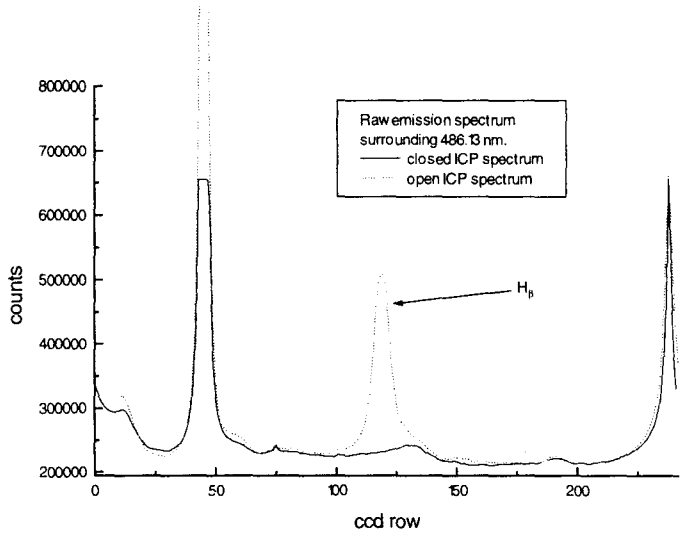

Figure 13. Spectrum around 486.13 nm; the wavelength of H_β emission. The dotted spectrum is that of an open argon ICP, the solid spectrum of a closed argon filled ICP, originally containing 0.025 volume % H_2. Water in the surroundings is probably the main reason for the presence of hydrogen in the open ICP. One CCD row corresponds to a 20 pm wavelength interval. The asymmetry in the H_B line shape is presumably caused by a weak transition in the right wing of the profile.

Clearly visible is the H_β emission in the open ICP, probably originating from atmospheric water and possibly some impurities in argon, although we are not interested in the source at this moment. Also visible is the similarity of the direct spectrum surrounding 486.13 nm. This leads to the conclusion that probably through diffusion of hydrogen into the quartz vessel walls, the amount of hydrogen in the vessel has fallen below the for our equipment detectable limit. The asymmetry in the H_B line shape is presumably caused by a weak transition in the right wing of the profile.

4.4.3 Power dependence

Using the results from ALI, DLA and LIPI, the power dependence of the plasmas with filling pressures 10, 50 and 100 mbar is investigated. The result from Thomson scattering T_e = 9300K ± 600K for the 100 mbar case at 100 W for r = 6 mm, is used to verify electron temperatures yielding from ALI.
For the 100 mbar case, Figure 14 shows the spatial ALI electron temperature behavior for four plasma powers 50, 75, 100 and 125 W.

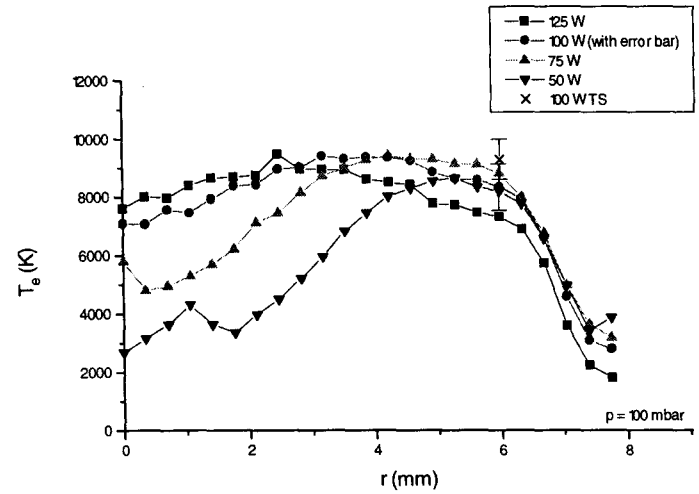

Figure 14. ALI electron temperatures spatially resolved for 50W, 75W, 100W and 125W at an argon filling pressure of 100 mbar. A TS point for 100 W case is marked with an 'x'.

This figure shows a decreasing torodial plasma structure for increasing plasma powers. The estimated margin of error in the temperatures is 20% (see Figure 4). The cross in Figure 14 shows T_e determined with Thomson scattering at 100 W plasma power: T_e = 9300K ± 600K. This is in agreement with the corresponding ALI value considering specified inaccuracies. Spatially resolved ALI electron densities for the 100 mbar case for the four plasma powers are depicted in Figure 15.

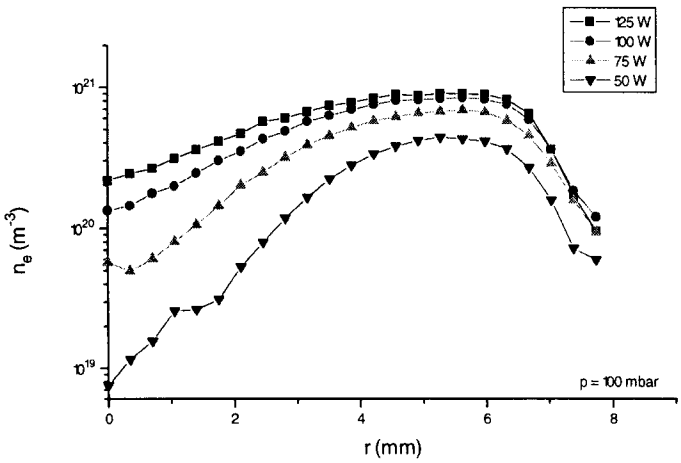

Figure 15. ALI electron densities spatially resolved for 50W, 75W, 100W and 125W at an argon filling pressure of 100 mbar.

An increase in the plasma power causes the electron density to increase. In this figure, the decreasingly pronounced torodial structure for increasing plasma powers as observed for T_e can also be observed. Peak values of the electron density profiles can be found around r = 5.5 mm. The estimated error margin is 15%.
For the 100 mbar case increase in plasma power is used for plasma expansion rather than for increase of electron temperatures above 9000-10000K.
ALI electron temperatures for the 10 mbar vessel at the four considered powers are illustrated in Figure 16. Differences with the 100 mbar case are striking.

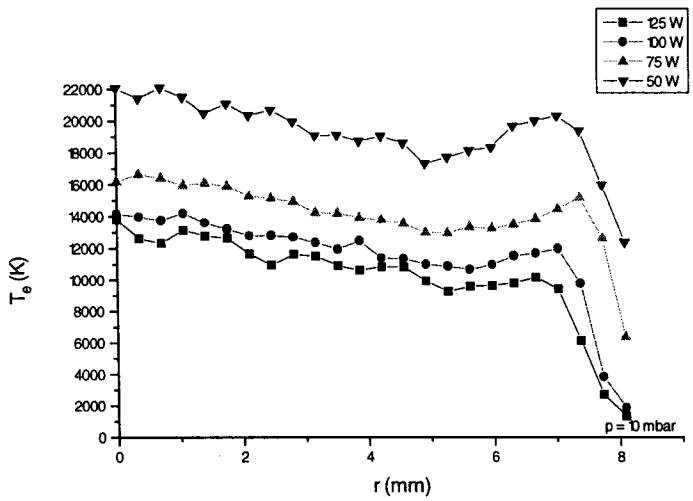

Figure 16. ALI electron temperatures spatially resolved for 50W, 75W, 100W and 125W at an argon filling pressure of 10 mbar.

The profiles no longer have a torodial structure. In contrast with the 100 mbar case the shape of the temperature profile has become insensitive to power changes, but the profile as a

whole now shows great sensitivity to power. Remarkable is the direction of the power behavior: Electron temperatures decrease for increasing plasma powers. The estimated error margin is from 25% for temperatures around 11000 K up to 40% for temperatures around 20000 K.
A complete absence of a torodial structure shows in the ALI electron density profiles as presented in Figure 17. Here we notice that electron densities are almost independent of plasma power. The margin of error is 15%.

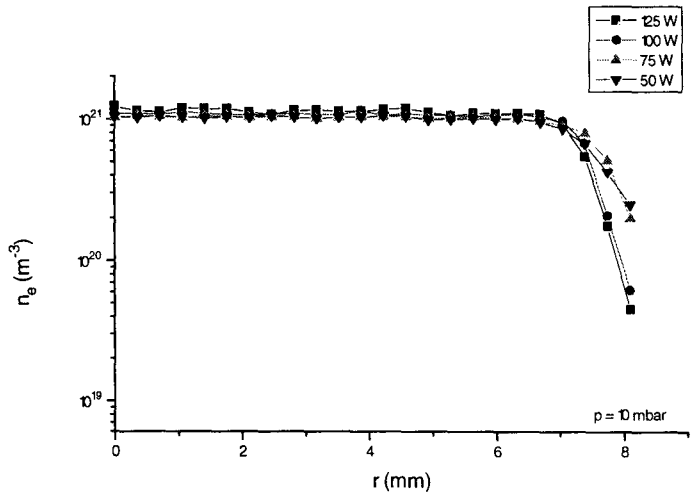

Figure 17. ALI electron densities spatially resolved for 50W, 75W, 100W and 125W at an argon filling pressure of 10 mbar.

An indication for an explanation of the decreasing T_e for increased power can be found when T_h power behavior for the 10 mbar case is shown in Figure 18. T_h profiles result from DLA, the margin of error in T_h is 500K.

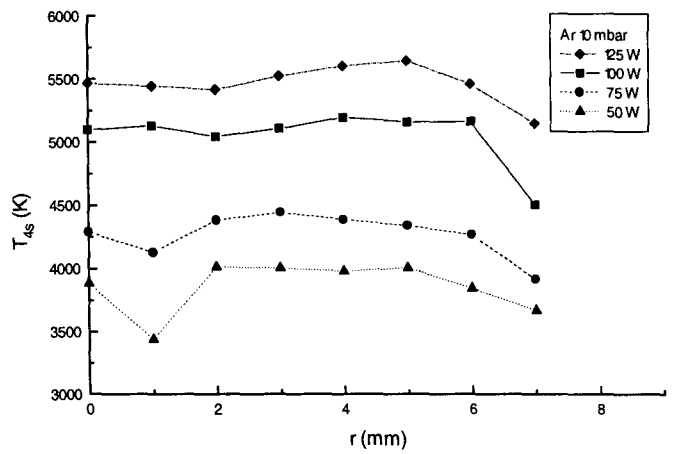

Figure 18. DLA heavy particle temperatures spatially resolved, calculated from the Gaussian component of the absorption profiles. These profiles result from measurements on an argon filled vessel with filling pressure 10 mbar, for plasma powers of 50W, 75W, 100W and 125W.

The behavior of T_h as determined with DLA shows an increase of T_h with plasma power. In case of a *closed* ICP, increase in T_h corresponds to the increase of pressure, and therefore of kinetic energy density. Apparently this allows the plasma to be sustained at a lower electron temperature.
The $4s^3P_2$ population density profiles from DLA are given in Figure 19.

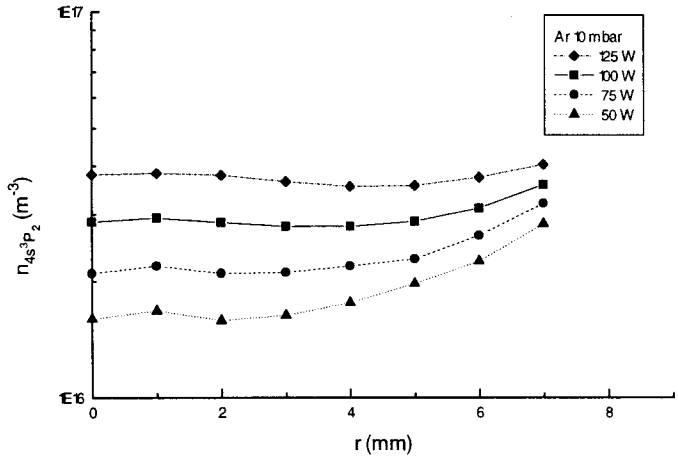

Figure 19. DLA $4s^3P_2$ population densities spatially resolved calculated from the integrated absorption profiles. These profiles result from measurements on an argon filled vessel with filling pressure 10 mbar, and applied plasma powers of 50W, 75W, 100W and 125W. The statistical weight of this state is 5.

The estimated margin of error is 15%. An increase of the densities is seen for increasing plasma power. Also noticeable is the increase of density towards the plasma vessel walls at 8 mm. This behavior is to be expected, since heavy particle temperatures drop for increasing radius causing Ar ground state densities to increase, and electron densities more or less stay the same. Figure 20 presents the radial ALI electron temperature profiles of the 50 mbar vessel. The power behavior is roughly a mix between the 100 mbar and the 10 mbar case. For increasing powers we notice an increasingly less pronounced profile and at the same time the decreasing T_e behavior is visible around r = 5 mm. The margin of error is 20%.

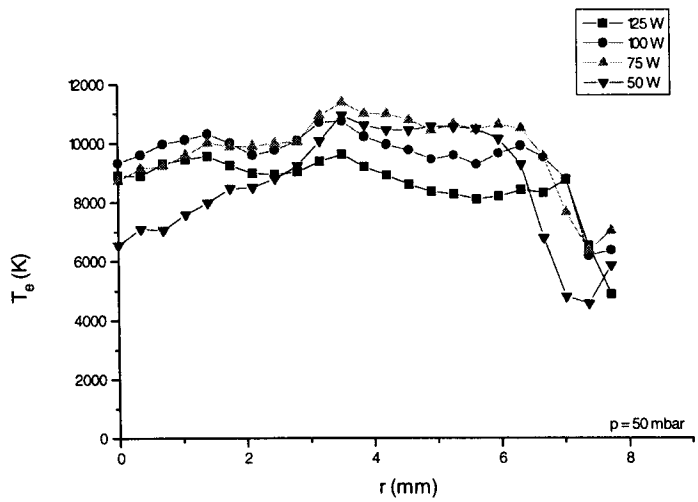

Figure 20. ALI electron temperatures spatially resolved for 50W, 75W, 100W and 125W at an argon filling pressure of 50 mbar.

The ALI electron density profiles Figure 21 for the 50 mbar also show aspects of both the 100 mbar and the 10 mbar case. The profiles are clearly less pronounced torodial than in the 100 mbar case, and still show more increase with increase of power than in the 10 mbar case. The estimated margin of error is 15%.

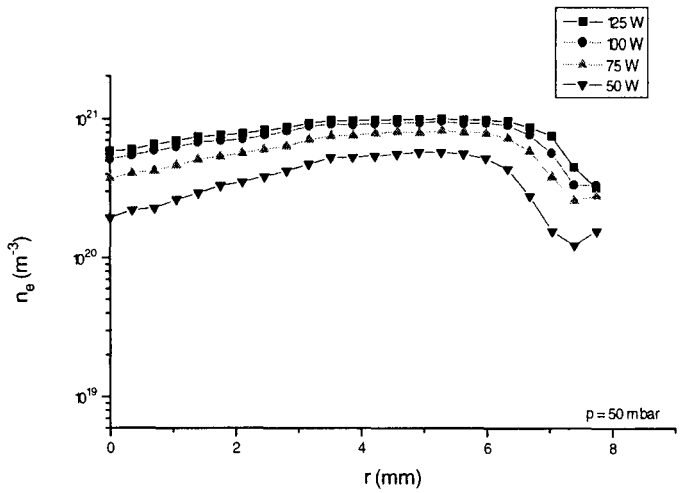

Figure 21. ALI electron densities spatially resolved for 50W, 75W, 100W and 125W at an argon filling pressure of 50 mbar.

4.4.4 Filling pressure dependence

For a plasma power of 100 W, the behavior of the plasma as a function of the different argon filling pressures of 10 mbar, 50 mbar and 100 mbar at room temperature is investigated using ALI, LIPI, and DLA. Figure 22 shows the electron density dependence on filling pressure.

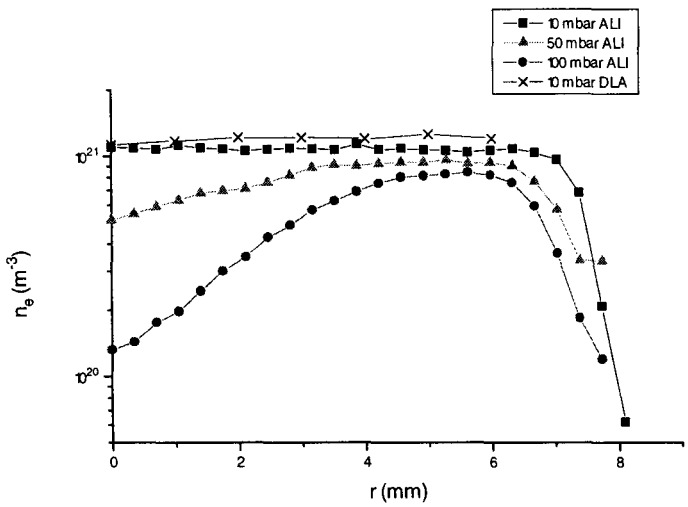

Figure 22. ALI and DLA electron densities spatially resolved for plasma power 100 W, filling pressures 10, 50 and 100 mbar.

The shape of the electron density profile determined with DLA for 10 mbar is similar to that determined with ALI. n_e Values based on DLA are 10-15% higher than ALI values. A possible explanation for this is the possible influence of Van der Waals broadening, also contributing to the Lorentzian component of the absorption profile shape.
It is clear that for decreasing filling pressures, the electron density profile gets increasingly flat. The explanation for this behavior can be found with electron diffusion, not with EM field coupling with the plasma; the skin depth δ of an EM field with frequency ω is given by

$$\delta = \sqrt{\frac{2}{\mu_0 \sigma \omega}} \qquad (10)$$

with σ the electrical conductivity, proportional with $T_e^{3/2}$, and therefore decreasing with increasing filling pressures since electron temperatures decrease with increasing filling pressures (Figure 23). From (10) follows then that the skin depth in the 10 mbar case is smaller than in the 100 mbar case.

Electron diffusion is proportional to the free mean path λ_v of electrons in the plasma. For increasing filling pressures, λ_v decreases because of the increased background particle density, and therefore the 'leveling out effect' because of diffusion at a given gradient in n_e decreases. This allows the existence of more pronounced n_e profiles for increasing filling pressures, as observed in the experiments.

Figure 23 shows a different profile dependence of pressure than n_e. The shape of the profiles does not change as dramatically; the dependence is mainly reflected in the magnitude of T_e.

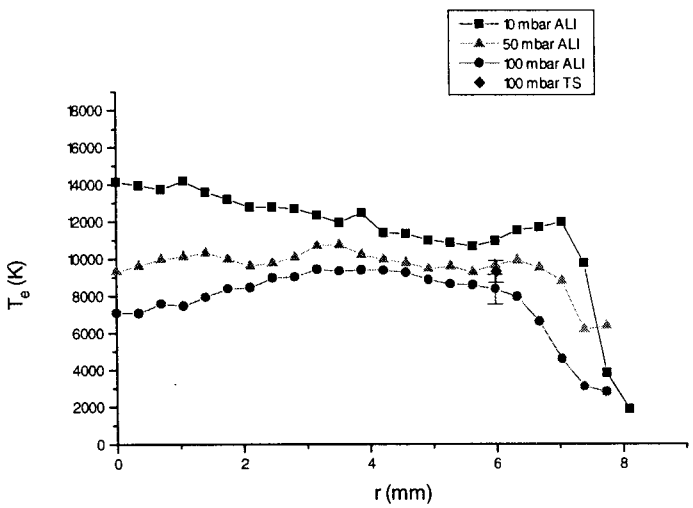

Figure 23. ALI electron temperatures spatially resolved for plasma power 100 W, filling pressures 10, 50 and 100 mbar. For the 100 mbar case, the TS electron temperature at 6 mm is added for verification.

For higher filling pressure, we find a decreasing electron temperature. This can be explained by an improved coupling between electrons and heavy particles, reducing the temperature difference between them. This view is confirmed by LIPI experiments, of which results are displayed in Figure 24.

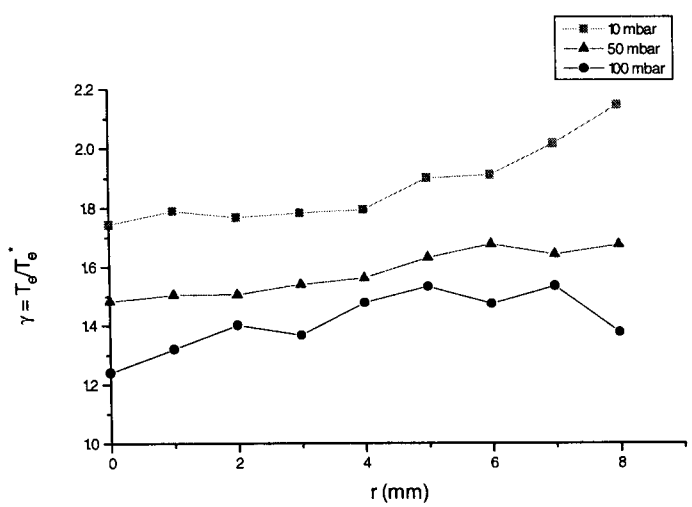

Figure 24. LIPI γ-profiles for plasma power 100 W, and filling pressures 10, 50 and 100 mbar.

Although T_e^* is an upper limit for the real heavy particle temperature, the trend in the figure is clear and shows an decreased ratio for increased filling pressures.
The electron temperatures yielding from ALI (Figure 23) are divided by the ratio T_e/T_e^* (Figure 24) to obtain T_e^* , the upper limit estimations of T_h. These limits are depicted in Figure 25, together with heavy particle temperatures obtained with DLA for the 10 mbar case.

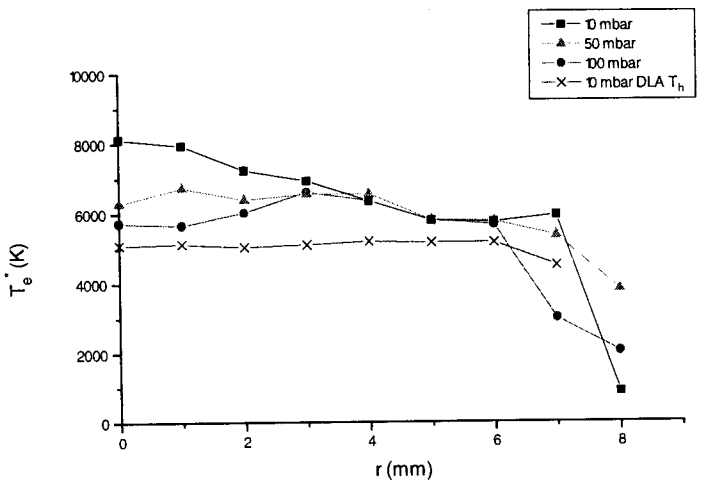

Figure 25. Upper limits of T_h derived from ALI T_e values divided by LIPI γ values. The crossed line indicates DLA T_h values for the 10 mbar case.

This figure does show that DLA heavy particle temperatures T_h are indeed lower than T_e^* for the 10 mbar case. DLA experiments on 50 mbar and 100 mbar vessels *indicate* that this is also the case for these higher filling pressures, see Figure 26.

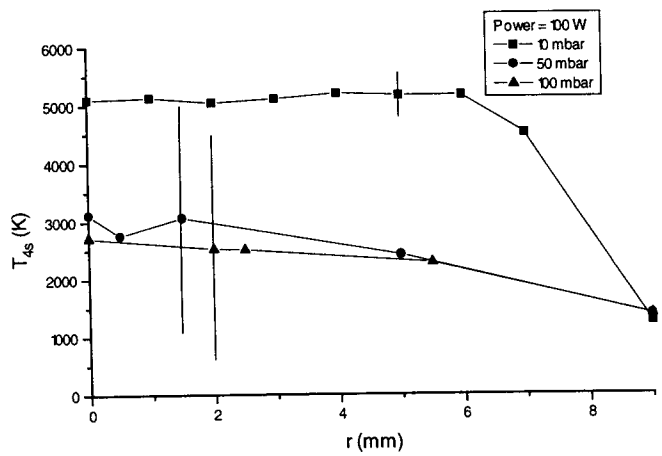

Figure 26. DLA heavy particle temperatures spatially resolved, calculated from the Gaussian component of the absorption profiles. These profiles result from measurements on argon filled vessels with filling pressures of 10, 50 and 100 mbar at plasma power 100W.

The reason for the fact that the T_h values for 50 mbar and 100 mbar can only be regarded as indications, is caused by interference of the laser beam with internal reflections in the quartz walls of the plasma vessel and interference from reflections between the vessel walls as illustrated in Figure 27.

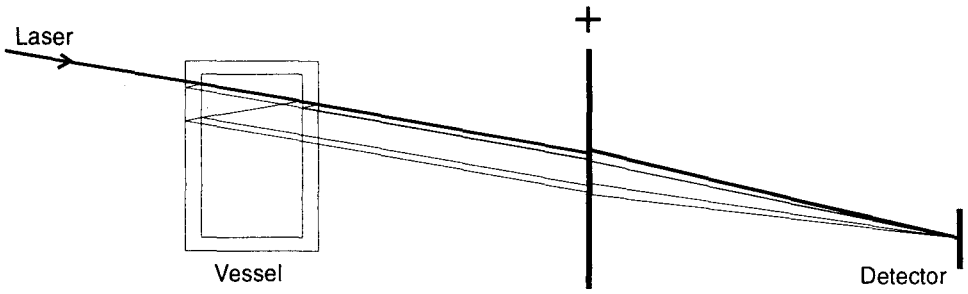

Figure 27. Several likely ways of interference affecting the ability to determine the absorption coefficients of the plasma. Only up to second order reflections are drawn.

For the 100 mbar and the 50 mbar vessels, the geometry of the vessel changes by an amount of order 1 μm per few seconds typically, causing the resulting detected laser beam to change in amplitude. This change in amplitude is comparable to the absorbed fraction of the beam. Since a laser wavelength scan over the complete absorption profile takes a few seconds, the shape of the absorption profile is badly affected by this interference effect. Decreasing the scan time would be the obvious solution. Unfortunately, the scan time is limited by the characteristic thermal heating time of the laser device since changing the laser wavelength is obtained by internally heating of the device by ohmic dissipation, causing the laser cavity size to vary. This interference effect plays a less important role in the 10 mbar case, probably because coupling of energy to the vessel wall is a more homogeneous process because of the less pronounced toroidal structure of the plasma. The result is that the estimated margin of error on the 50 mbar and 100 mbar T_h values is 2000K, and for 10 mbar 500K.

4.5 Conclusions

In the investigation of closed argon filled ICP's with filling pressures 10, 50 and 100 mbar, ALI proves to be the most versatile diagnostic, providing results electron density and temperature profiles for all filling pressures and plasma powers. LIPI is also generally applicable, but only adds upper limit estimations for the real heavy particle temperatures, because electrons are heated by three particle recombination above the heavy particle temperature. The only 'direct way' to determine heavy particle temperatures is DLA, and this technique is, because of the variation in interference for 50 and 100 mbar vessels, only applicable for the 10 mbar case (all powers). Where techniques overlap, they generally provide results that are in agreement given the specified error margins.

For 100 mbar filling pressure, electron temperature profiles flatten for increased power, and their maximum values are more or less power independent. Electron density profiles also flatten for increasing power, whereas their maximum values increase.

For 10 mbar filling pressure, the shape of electron temperature profiles is power independent, and electron temperatures decrease for increasing power. Electron density profiles are completely flat, and independent of power. Heavy particle temperatures increase with power, and the shape of the profiles is power independent. The population of the argon 4s-state increases for increasing powers and tends to increase towards the plasma walls.

For 50 mbar filling pressure, plasma power behavior appears to have aspects of both 10 mbar and 100 mbar filling pressures.

For constant plasma power of 100 W, we observe a strong flattening of the electron density profile for decreasing filling pressure. The shape of the electron temperature profiles is only weakly affected by filling pressure, but the magnitude of electron temperatures decreases

with increasing plasma power. DLA and LIPI experiments both suggest an improved electron-heavy patricle coupling for increased filling pressure.

---

[1] F.H.A.G. Fey. 'Excitation Balances and Transport in an inductively coupled Plasma', Thesis 1993.
[2] J.M. de Regt. 'Fundamentals of inductively coupled argon plasmas', Thesis 1996.
[3] J.M. de Regt, F.P.J. de Groote, J.A.M.vd Mullen, D.C. Schram, 'Comparison of active and passive spectroscopical methods to investigate atmospheric plasmas', to be published, 1995.
[4] J.M.de Regt, R.D.Tas and J.A.M. vd Mullen and D.C.Schram,'A closed Inductively Coupled Plasma for lighting purposes mapped by spectroscopical techniques', submitted for publication to J.Phys.D:Appl. Phys.
[5] J.M.de Regt, R.D.Tas and J.A.M. vd Mullen. 'A diode laser absorption study on a 100 Mhz argon Inductively Coupled Plasma', Journal of Physics D: Applied Physics, submitted for publication to J. Phys. D: Appl. Phys., 1995.
[6] V.M.Lelevkin, D.K.Otorbaev, D.C.Schram, 'Physics of non-equilibtium plasmas'.
[7] J.M.de Regt, R.A.H. Engeln, F.P.J. de Groote, J.A.M. van der Mullen and D.C. Schram, 'Thomson scattering experiments on a 100 Mhz ICP calibrated by Raman scattering', Review of Scientific Instruments 66 (332), 1995.
[8] F.P.J. de Groote, 'Diagnostic tools for atmospheric plasmas compared', MS work VDF/NT 95-27.
[9] H.R.Griem, A.C.Kolb and K.Y.Shen, Phys.Rev. 116, 4 (1959).
[10] V.Helbig and K-P.Nick, J.Phys.B 14, 3573 (1981).

General conclusions

This report shows three stages in a research project aimed at the acquisition of insight in closed inductively coupled argon plasmas. A multi channel ALI device for obtaining spatially resolved atomic state population densities in the plasma has been constructed. In order to use this device to determine spatially resolved electron densities and temperatures in the plasmas, more accurate transition probabilities have been determined with the McALI device in combination with Thomson scattering. Here, an open argon ICP was used as plasma source. With these new transition probabilities, McALI has been successfully used to determine spatially resolved electron densities and temperatures in the closed ICPs. Spatially resolved heavy particle temperatures, electron temperatures after power interruption and $4s^3P_2$ population densities using DLA and LIPI have been determined. A number of conclusions can drawn from the project.

- Crucial in the acquisition of spatially resolved electron temperatures and electron densities is the two dimensional CCD. We have shown that similar measurements with a PMT would take at least 75 times longer (resulting in about 18 hours per plasma condition). For accurate determination of emission line background radiation, wavelength resolved information is indispensable, especially for the very widened emission lines (FWHM > 1 nm) close to ionization. Finally, CCD detection limits are excellent compared to other diagnostics, especially for increasing spatial resolution.

- In order to obtain electron density and electron temperature profiles with McALI, accurate transition probabilities with initial state populations in pLSE are necessary. With McALI and TS on an open argon ICP, 15 transition probabilities are determined with inaccuracies within 20%, whereas the original inaccuracies were up to more than 50%.

- Measurements on closed ICPs show that electron temperature and electron density behavior as function of plasma power is strongly influenced by filling pressure. For increasing filling pressures an increased torodial plasma structure in the electron density profiles is observed. Electron temperatures decrease for increasing filling pressures.

- The combination of several diagnostical techniques, some yielding the same plasma quantities, is essential to determine whether the diagnostic is producing correct results and leeds to a deeper understanding of the techniques.

Appendix

This appendix lists the Pascal library interface of the unit TASCOM.PAS that contains pascal functions corresponding to ST6 camera functions. It uses the unit RS232_3.PAS for low-level port communication with the camera. The unit TASCOM.PAS is used by the lab experimentation user program ICP30.PAS via the shell CS_PROC.PAS.

```
{-------------------------------------------------------------------------}
{     ST6-UV library version 1.0                                          }
{     This unit contains functions to all of                              }
{     the commands of the ST6-UV camera except for the                    }
{     aux-port functions.                                                 }
{     Written by R.D.Tas feb. 1995.                                       }
{-------------------------------------------------------------------------}

unit tascom;

interface
uses crt,rs232_3;

const MAXNROFPIXELS = 2048;
    DARK_BUF = 0;
    LIGHT_BUF = 1;
    ACC_BUF  = 2;
    SH_CICR  = 0;
    SH_OICR  = 1;
    SH_OIOR  = 2;
    TURBOVISION = 1;
    STDPASCAL = 2;
    MAXMODE = 9;

var mode750,show_errors:boolean;
   st6Platform:word;
   xymode:array[0..MAXMODE,0..1] of integer;

type LINEARR = array[0..MAXNROFPIXELS] of word;
type LINERARR = array[0..MAXNROFPIXELS] of real;

function reset_st6:integer;
function shutter_open:integer;
function shutter_shut:integer;
function set_com_baud(baudrate:longint):integer;
function get_rom_version(var version:word):integer;
function get_activity_status(command:word):integer;
function take_image( exp_time:longint; line_start, lines, pixel_start, pixels,
                enable_dcs, dc_restore, abg_state, abg_period,
                destbuf, darksubtr, mode, shutter:word ):integer;
function end_exposure:integer;
function abort_exposure:integer;
```

```
function set_head_offset(offset:word):integer;
function read_blank_video(enable_dcs,offset:word; var video:word ):integer;
function flush_ccd(times:word):integer;
function clr_buf(buffer:word):integer;
function get_uncompressed_line(buffer,firstline,firstpixel,nrofpixels:word; var
line:LINEARR):integer;
function get_readout_peak(var peakval,x,y:word):integer;
function cal_width(buffer,x0,y0,xwidth,ywidth:word; var width,height:word):integer;
function cal_cent(buffer,x0,y0,xwidth,ywidth:word; var cx,cy,sum:longint):integer;
function reduce_image(buffer:word):integer;
function shrink_image(buffer:word):integer;
function accum_image(xoff,yoff:word):integer;
function sub_offset(buffer,offset:word):integer;
function get_minmax(buffer,x0,y0,xwidth,ywidth:word;
          var minx,miny,minval,maxx,maxy,maxval:word ):integer;
function sub_dark:integer;
function activate_relay(txp,txm,typ,tym,tal:word):integer;
function enable_temp(temp:real):integer;
function disable_temp:integer;
function output_temp(tedriveval:word):integer;
function read_thermistor(var temp:real):integer;
function get_temp_status(var
enabled,setpoint,output,samp_rate,p_gain,i_gain,brownout:word):integer;
function get_cpu_info(var version,cpu,firmware_version:word;
                name:string;
                has_shutter,needs_offset,var_dcs,var_dcr,has_tcnt,
                max_te_drive,image_width,image_height,readout_modes,
                mode,width,height,gain:word;
                pwidth,pheight:longint):integer;
function get_result_buf(var comm:word; var buffer:BUFARR):integer;
function call_remote(segment,offset:word):integer;
function write_block(offset,segment,nrofbytes:word; buffer:BUFARR):integer;
function read_block(offset,segment:word; var nob:word; var buffer:BUFARR):integer;
function find_head_offset:integer;
function first_com(baudrate:longint):integer;
function last_com:integer;
procedure error(s1,s2:string);

implementation
```

Dankwoord

Met heel veel plezier heb ik mijn afstudeer onderzoek kunnen doen in het ICP lab van de groep van Daan Schram. Daan wil ik van harte bedanken voor het gesprek dat wij hadden ruim twee jaar geleden in een 747 naar de V.S. Dit heeft mij doen besluiten om in deze groep mijn studie af te maken.
Erg aangenaam was de samenwerking met 'ICP boss' Hans de Regt, die een zeer stimulerende omgeving creeerde en soms voor de nodige ordening zorgde, en samen met Joost van der Mullen (Joost mag het weten) voor een geweldige begeleiding in dit onderzoek zorgden. Ook met Frank de Groote en Jan van Dijk heb ik met plezier samengewerkt.
Verder bedank ik iedereen waar ik regelmatig mee om ga voor het scheppen van een ideale sfeer, waarin bijzonder goed gewerkt kan worden. Hans, Joost, Jeroen, Ger, Richard, Frank, Jan, Rene, Dany, Seth, Ralph, Roger, Judith, Ries, Herman, Bertus, ontzettend bedankt.
Ook wil ik onze Philips contacten hartelijk bedanken voor de vele interessante discussies die we hadden gedurende dit project. Achim koerber, Pieter Postma en Johan van Vliet bedankt.
En dan last but certainly not least Rebecca for TLC during these years.